J. Mech. Phys. Solids 176 (2023) 105302

Contents lists available at ScienceDirect

Journal of the Mechanics and Physics of Solids

journal homepage: www.elsevier.com/locate/jmps

A mechanism-based multisurface plasticity model for hexagonal close-packed materials with detailed validation and assessment

Padmeya P. Indurkar [a,b], Shailendra P. Joshi [b,*]

[a] Department of Mechanical Engineering, National University of Singapore, Singapore
[b] Department of Mechanical Engineering, University of Houston, Houston, TX 77204, USA

ARTICLE INFO

Keywords:
HCP materials
Magnesium and Mg alloys
Multisurface model (MSM) of plasticity
Glide and twinning

ABSTRACT

We present a multi-surface model (MSM) of plasticity to simulate the anisotropic and asymmetric yield responses often observed in hexagonal close-packed (HCP) materials such as magnesium and its alloys. Motivated by the salient outcomes from high-resolution polycrystal plasticity simulations and experimental insights on magnesium alloys, we propose a three-surface representation incorporating two separate anisotropic, symmetric yield surfaces for the soft (basal) and hard (non-basal) glide, and an anisotropic, asymmetric yield surface for extension twinning. This reduced representation of the high-resolution crystal plasticity offers computational attractiveness to analyze large-scale engineering simulations while maintaining key micromechanical details of soft versus hard glide. The model is calibrated to a particular three-dimensional dataset for polycrystal magnesium alloy and is validated against a range of crystal plasticity results for different loading conditions. The capability of the model is then assessed for complex boundary-value problems at the macroscale (round notched bars) and at the microscale (void growth and coalescence). The validation and assessment demonstrate the ability of the proposed MSM to capture finer details of deformation such as identifying regions where soft and hard glide may occur around the void or in other heterogeneous loading states.

1. Introduction

Many hexagonal close-packed (HCP) materials such as magnesium (Mg) and Mg alloys exhibit plastic anisotropy and tension–compression asymmetry. The extents of the plastic anisotropy and asymmetry depend on the microstructural features including grain size and texture, which are controlled by processing. Moreover, these behaviors evolve with progressive deformation. There has been a continuing interest in modeling the anisotropic and asymmetric plasticity of such materials using homogenization-based continuum plasticity theories. Since the seminal work on anisotropic plasticity theory by Hill (1948) (referred to here as HILL), noteworthy developments in accounting for tension–compression asymmetry include the single-surface models (SSM) by Cazacu and colleagues (Cazacu et al., 2006; Plunkett et al., 2008) (referred to here as CAZ06 and CAZ08 respectively), and have been shown to work in several applications including zirconium (Plunkett et al., 2006, 2007), α−Ti (Nixon et al., 2010a,b; Revil-Baudard et al., 2015), and magnesium alloy (Yoon et al., 2013; Chandola et al., 2015; Tari et al., 2014). However, there are some key unresolved challenges associated with SSMs. The main issue is that they cannot naturally account for the *evolution* of plastic anisotropy and tension–compression asymmetry. They require calibration of the material parameters at a fixed level of applied strain and by way of consequence, the same parameters need to be re-calibrated at multiple strain levels. Another difficulty is that it is not possible to resolve the plastic flow into different constitutive components. Both these issues can limit their utility for situations where

* Corresponding author.
E-mail address: shailendra@uh.edu (S.P. Joshi).

https://doi.org/10.1016/j.jmps.2023.105302
Received 2 October 2022; Received in revised form 7 March 2023; Accepted 18 April 2023
Available online 28 April 2023

plastic anisotropy and tension–compression asymmetry evolution is significant, as is often the case with magnesium and its alloys. Modifications to these models (see e.g., Yoon et al. (2013), Tari et al. (2014) and Muhammad et al. (2015)) typically result in a significant increase in the set of calibration parameters, and may not guarantee convexity of the yield function (Kondori et al., 2019). Based on the work of Lee et al. (2008), a notable effort in capturing the evolving plastic anisotropy and tension–compression asymmetry of HCP materials is by Li et al. (2010) that adopts a modified von Mises criterion with an initial non-zero back stress to account for asymmetry with combined isotropic–kinematic hardening. To evolve the asymmetry, an effective texture evolution is mapped using a weighted discrete probability density function of $\langle c \rangle$-axes orientations. The orientation of $\langle c \rangle$-axes evolves with twinning/detwinning using predefined rules.

In contrast to SSMs, a class of multi-surface models (MSM) have been proposed. They adopt different yield surfaces representing different plasticity modes such that their intersection gives an *effective* yield surface. Notable developments include the multisurface models by Kim and colleagues (Kim et al., 2013; Lee et al., 2017), which incorporate plastic anisotropy (HILL) and asymmetry (CAZ06). Steglich et al. (2016) propose a two-surface model: one yield surface (Barlat et al., 1991, BAR91) representing dislocation glide and the other incorporating a twinning affected mode (via CAZ06), which shows promise for a range of boundary value problems including uniaxial tension and compression (Lee et al., 2018; Kondori et al., 2019) and shear, tube compression and three-point bending of Mg alloy specimens (Lee et al., 2018). An attractive of feature these models is that they embed physically justifiable constitutive hardening rules that capture the evolution of plastic anisotropy and tension–compression asymmetry. Yet, some limitations persist. While the two-surface model adopts a computationally efficient single anisotropic yield surface to represent the soft and hard glide modes, it may not be adequate to represent the disparate nature of slip (the soft (basal) and hard (non-basal)) modes that prevail. In most Mg alloys, for instance, the soft (basal) glide is significantly softer compared to the hard glide modes. In pure Mg, basal slip ($\tau_0 \approx 0.5$ MPa) is typically to two orders of magnitude softer than pyramidal $\langle c + a \rangle$ slip ($\tau_0 \approx 40$ MPa). Moreover, these modes exhibit distinct self- and latent-hardening behaviors (Kelley and Hosford, 1967; Zhang and Joshi, 2012), which play a role in materials experiencing highly heterogeneous stress states. Such situations routinely arise, among other, in notched bars (Kondori and Benzerga, 2014; Selvarajou et al., 2017), indentation (Shin et al., 2013; Selvarajou et al., 2014), voided microstructures (Nemcko et al., 2016; Selvarajou et al., 2019). Moreover, they may have implications on failure. For example, basal slip may trigger macroscopic shear instability or microcracking (Koike and Ohyama, 2005; Ando et al., 2014). In contrast, the plastically hard prismatic and pyramidal slip modes may contribute to the ductile processes of void growth (Crépin et al., 1996; Nemcko and Wilkinson, 2016; Nemcko et al., 2016). It is not clear if and how such disparate effects can be captured without separating the mechanistic details of the soft and hard glide modes. The reduced crystal plasticity model proposed by Becker and Lloyd (2016) accounts for the disparate nature of soft and hard slip modes albeit at the grain scale, unlike the preceding models that are implied to simulate the homogenized responses at the specimen scale.

In this work, we present a three-surface model for HCP materials that deform by slip and twinning with the goal of more adequate accounting of the soft and hard glide modes. One HILL anisotropic yield surface accounts for the soft (basal) glide and another HILL yield surface for the hard (prismatic $\langle a \rangle$, pyramidal $\langle a \rangle$ and pyramidal $\langle c + a \rangle$) glide. The third yield surface (CAZ06), which is both anisotropic and asymmetric accounts for twinning. A collateral effect of this modification is the increased number of constitutive parameters compared to the two-surface model albeit with the potential to model the mechanical behaviors under complex stress states. The model is applied to a range of boundary value problems including uniaxial, shear, and triaxial stress states. Finally, the model is also applied to assess the micromechanics of void growth under controlled stress triaxiality. In each of these problems, the emergent interaction between the glide and twinning is assessed against experiments and finer scale (crystal plasticity) simulations. In the following, we present the theoretical formulation of a viscoplastic three-surface MSM for HCP metals with evolving plastic anisotropy and asymmetry, its computational implementation, validation of the calibrated model for a particular texture, and a comprehensive assessment of the model for a range of boundary value problems.

2. Theoretical formulation

2.1. Kinematics and kinetics

Given a material point $\boldsymbol{X}$ and its spatial coordinate $\boldsymbol{x}(t)$ at time t, the total deformation gradient is $\mathbf{F} = \partial \boldsymbol{x}/\partial \boldsymbol{X}$, and the total velocity gradient $\mathbf{L}$ is $\mathbf{L} = \dot{\mathbf{F}}\mathbf{F}^{-1}$ where the overdot represents the material time derivative. Further, $\mathbf{L}$ is additively decomposed into a symmetric part $\mathbf{D}$ (rate-of- deformation) and a skew-symmetric part $\boldsymbol{\Omega}$ (continuum spin), $\mathbf{L} = \mathbf{D} + \boldsymbol{\Omega}$. Then,

$$\mathbf{D} = \mathbf{D}_e + \mathbf{D}_p \tag{1}$$

where $\mathbf{D}_e = \mathbb{L}^{-1} : \dot{\boldsymbol{\sigma}}_J$ is the elastic rate of deformation with $\mathbb{L}$ the fourth-order elastic moduli tensor and $\dot{\boldsymbol{\sigma}}_J$ is the Jaumann rate of Cauchy stress, which is related to the total rate of Cauchy stress $\dot{\boldsymbol{\sigma}}$ via $\dot{\boldsymbol{\sigma}}_J = \dot{\boldsymbol{\sigma}} + \boldsymbol{\sigma}\boldsymbol{\Omega} - \boldsymbol{\Omega}\boldsymbol{\sigma}$.

The total plastic rate of deformation $\mathbf{D}_p$ is assumed to have three contributions: (i) soft plasticity $\left(\mathbf{D}_p^s\right)$, (ii) hard plasticity $\left(\mathbf{D}_p^h\right)$, and (iii) twinning plasticity $\left(\mathbf{D}_p^{tw}\right)$ so that $\mathbf{D}_p = \mathbf{D}_p^s + \mathbf{D}_p^h + \mathbf{D}_p^{tw}$.

Assuming the normality rule, these sub-terms are defined by their corresponding yield functions as:

$$\mathbf{D}_p^s = \dot{\bar{\varepsilon}}^s \frac{\partial \mathcal{F}^s(\boldsymbol{\sigma})}{\partial \boldsymbol{\sigma}} \quad , \quad \mathbf{D}_p^h = \dot{\bar{\varepsilon}}^h \frac{\partial \mathcal{F}^h(\boldsymbol{\sigma})}{\partial \boldsymbol{\sigma}} \quad \text{and} \quad \mathbf{D}_p^{tw} = \dot{\bar{\varepsilon}}^{tw} \frac{\partial \mathcal{F}^{tw}(\boldsymbol{\sigma})}{\partial \boldsymbol{\sigma}} \tag{2}$$

where the yield functions

$$\mathcal{F}^s = \bar{\sigma}^s - g^s \quad ; \quad \mathcal{F}^h = \bar{\sigma}^h - g^h \quad ; \quad \mathcal{F}^{tw} = \bar{\sigma}^{tw} - g^{tw} \tag{3}$$

are described in terms of the current equivalent stress for each mode, $\bar{\sigma}^i$ $(i = s, h, tw)$, and the corresponding current strength g^i. The effective plastic strain rate, $\dot{\bar{\varepsilon}}^i$ for the ith mode, is prescribed as a power-law function:

$$\dot{\bar{\varepsilon}}^i = \dot{\varepsilon}_0^i \left[\frac{\bar{\sigma}^i}{g^i}\right]^{1/m^i} \tag{4}$$

where $\dot{\varepsilon}_0^i$ is the characteristic strain rate and m^i is the strain-rate sensitivity parameter.

In Eq. (3), $\mathcal{F}^s$ and $\mathcal{F}^h$ are symmetric (HILL) yield functions while $\mathcal{F}^{tw}$ incorporates tension–compression asymmetry (via CAZ06). Next, the basic features of these yield surfaces are described.

2.2. Soft and hard plasticity modes

Following Benzerga and Besson (2001), the HILL representations for the soft (s) and hard (h) plasticity modes are written as:

$$\bar{\sigma}^s(\boldsymbol{\sigma}, \mathbb{h}^s) = \left[\frac{3}{2}\boldsymbol{\sigma}' : \mathbb{h}^s : \boldsymbol{\sigma}'\right]^{1/2} \quad \text{and} \quad \bar{\sigma}^h(\boldsymbol{\sigma}, \mathbb{h}^h) = \left[\frac{3}{2}\boldsymbol{\sigma}' : \mathbb{h}^h : \boldsymbol{\sigma}'\right]^{1/2} \tag{5}$$

where $\mathbb{h}^s$ and $\mathbb{h}^h$ are the fourth-order Hill-anisotropy tensors for the soft and hard plasticity modes, respectively. In general, the matrix of $\mathbb{h}$ may comprise both, diagonal and off-diagonal terms. For a plastically orthotropic material with principal material directions L-T-S, $\mathbb{h}$ is a diagonal matrix whose components (in Voigt notation) are $\mathbb{h}^i = \{h^i_{\mathsf{L}}, h^i_{\mathsf{T}}, h^i_{\mathsf{S}}, h^i_{\mathsf{TS}}, h^i_{\mathsf{LS}}, h^i_{\mathsf{LT}}\}$ where $i = s$ or h. Note that $\mathbb{h}$ is symmetric positive definite, so that $h_{ijkl} = h_{jikl} = h_{ijlk} = h_{klij}$ and $\boldsymbol{\sigma} : \mathbb{h} : \boldsymbol{\sigma} > 0, \forall\, \boldsymbol{\sigma} \neq \mathbf{0}$.

Let σ_0^s be the initial yield stress of the soft mode. Upon yielding, the self- and latent-hardening arising from interactions between the different plasticity modes causes it to harden. These effects are accounted for in obtaining the current strength (g^s) as:

$$g^s\left(\bar{\varepsilon}^s,\ \bar{\varepsilon}^h,\ \bar{\varepsilon}^{tw}\right) = \sigma_0^s + \underbrace{\mathcal{H}^s\bar{\varepsilon}^s}_{\substack{\text{self}\\ \text{hardening}}} + \underbrace{\mathcal{H}_h^s\bar{\varepsilon}^h + \mathcal{H}_{tw}^s\bar{\varepsilon}^{tw}}_{\substack{\text{latent}\\ \text{hardening}}} \tag{6}$$

where $\mathcal{H}^s$, $\mathcal{H}_h^s$ and $\mathcal{H}_{tw}^s$ are material hardening parameters for the soft plasticity mode.

Likewise, for the hard plasticity mode with the initial yield stress σ_0^h, we propose:

$$g^h\left(\bar{\varepsilon}^s,\ \bar{\varepsilon}^h,\ \bar{\varepsilon}^{tw}\right) = \sigma_0^h + \underbrace{Q^h\left(1 - \exp\left(-b^h\bar{\varepsilon}^h\right)\right)}_{\substack{\text{Voce-type self}\\ \text{hardening}}} + \underbrace{\mathcal{H}_s^h\bar{\varepsilon}^s + \mathcal{H}_{tw}^h\bar{\varepsilon}^{tw}}_{\substack{\text{latent}\\ \text{hardening}}} \tag{7}$$

with $Q^h, b^h, \mathcal{H}_s^h$ and $\mathcal{H}_{tw}^h$ being its material hardening parameters.

2.3. Twinning plasticity mode

In the CAZ06 model, the effective stress for twinning is given by:

$$\bar{\sigma}^{tw}(\boldsymbol{\sigma}, \mathbb{C}, k, a) = B\left[\left(|s_1| - ks_1\right)^a + \left(|s_2| - ks_2\right)^a + \left(|s_3| - ks_3\right)^a\right]^{1/a} \tag{8}$$

where s_i are the principal values of $\boldsymbol{s} = \mathbb{C} : \mathbb{J} : \boldsymbol{\sigma}$ with $\mathbb{J}$ the deviatoric projection tensor, k controls the yield asymmetry and a controls the yield surface curvature. Convexity is guaranteed so long as $k \in [-1, 1]$ and integer $a \geq 1$. The linear transformation tensor $\mathbb{C}$ has nine independent parameters. For orthotropic plastic anisotropy (L-T-S), $\mathbb{C}$ is expressed as (using Voigt notation):

$$\mathbb{C}^{tw} = \begin{bmatrix} C^{tw}_{\mathsf{L}} & \hat{C}^{tw}_{\mathsf{LT}} & \hat{C}^{tw}_{\mathsf{LS}} & 0 & 0 & 0 \\ \hat{C}^{tw}_{\mathsf{LT}} & C^{tw}_{\mathsf{T}} & \hat{C}^{tw}_{\mathsf{TS}} & 0 & 0 & 0 \\ \hat{C}^{tw}_{\mathsf{LS}} & \hat{C}^{tw}_{\mathsf{TS}} & C^{tw}_{\mathsf{S}} & 0 & 0 & 0 \\ 0 & 0 & 0 & C^{tw}_{\mathsf{TS}} & 0 & 0 \\ 0 & 0 & 0 & 0 & C^{tw}_{\mathsf{LS}} & 0 \\ 0 & 0 & 0 & 0 & 0 & C^{tw}_{\mathsf{LT}} \end{bmatrix} \tag{9}$$

In Eq. (8), B is not an independent parameter but an implicit expression of parameters in $\mathbb{C}$, k and a, and is obtained by equating $\bar{\sigma}^{tw}$ to a reference material direction tensile flow stress (e.g., L), cf. Plunkett et al. (2008).

The twinning yield surface is assumed to harden as

$$g^{tw}\left(\bar{\varepsilon}^s,\ \bar{\varepsilon}^h,\ \bar{\varepsilon}^{tw}\right) = \sigma_0^{tw} + \underbrace{Q^{tw}\left(\exp\left(b^{tw}\bar{\varepsilon}^{tw}\right) - 1\right)}_{\substack{\text{Exponential (sigmoidal) self}\\ \text{hardening}}} + \underbrace{\mathcal{H}_s^{tw}\bar{\varepsilon}^s + \mathcal{H}_h^{tw}\bar{\varepsilon}^h}_{\substack{\text{latent}\\ \text{hardening}}} \tag{10}$$

where σ_0^{tw} is the initial yield stress. The second term in Eq. (10) accounts for twinning induced (sigmoidal) hardening while the latent hardening terms account for interaction with the glide modes.

The constitutive model described above is implemented in ABAQUS/STANDARD® via User MATerial (UMAT) subroutine. The computational implementation is presented in Appendix A.

Table 1
MSM parameters calibrated against CP data.

Plasticity modes		Calibrated parameters for textured polycrystal					
Soft glide	Hardening (MPa)	σ_0^s	$\mathcal{H}^s$	$\mathcal{H}_h^s$	$\mathcal{H}_{tw}^s$		
		215	7017	1500	1000		
	Anisotropy	h_{L}^s	h_{T}^s	h_{S}^s	h_{LT}^s	h_{LS}^s	h_{TS}^s
		0.98	1.7	0.41[b]	1.03	23.8	58.6
Hard glide	Hardening (MPa)	σ_0^h	Q^h	b^h	$\mathcal{H}_s^h$	$\mathcal{H}_{tw}^h$	
		83	164	36	0[a]	0[a]	
	Anisotropy	h_{L}^h	h_{T}^h	h_{S}^h	h_{LT}^h	h_{LS}^h	h_{TS}^h
		1.06	1.10	0.69[b]	1.27	1.60	1.64
Twinning	Hardening (MPa)	σ_0^{tw}	Q^{tw}	b^{tw}	$\mathcal{H}_s^{tw}$	$\mathcal{H}_h^{tw}$	
		89	1.83	65	5000	11 500	
	Anisotropy and Asymmetry	C_{L}^{tw}	C_{T}^{tw}	C_{S}^{tw}	C_{LT}^{tw}	C_{LS}^{tw}	C_{TS}^{tw}
		1[a]	0.76	−10.36	13.29	−2.18	−2.91
		$\hat{C}_{\mathsf{LT}}^{tw}$	$\hat{C}_{\mathsf{LS}}^{tw}$	$\hat{C}_{\mathsf{TS}}^{tw}$	k	a	
		13.25	0.285	−0.292	0.872	4[a]	

[a]Indicates fixed (assumed) parameters.
[b]Indicates dependent Hill coefficients.

3. Crystal plasticity dataset for MSM calibration

The model presented in Section 2 is calibrated against a particular polycrystal plasticity dataset from Indurkar et al. (2020). Fig. 1 consolidates salient information from that reference. Fig. 1(a) shows the computational domain with the principal material directions (L-T-S) and Fig. 1(b) shows the textural details as (0001) and $(10\bar{1}0)$ pole figures adopted to prescribe grain orientations to the 300 grains in the polycrystal; Figs. 1(c) and 1(d) show the uniaxial responses in tension and compression respectively along the principal material (L, T, S) and off-axis (i.e., 45°) directions (LT, TS, and LS) signifying the response anisotropy and tension–compression asymmetry. The MSM material parameter set calibrated to these dataset are: $\mathcal{Y} \in \{\mathcal{Y}_s, \mathcal{Y}_h, \mathcal{Y}_{tw}^{\text{hard}}, \mathcal{Y}_{tw}^{\text{yield}}\}$ where $\mathcal{Y}_s = \{\sigma_0^s, \mathcal{H}^s, \mathcal{H}_h^s, \mathcal{H}_{tw}^s, h_{\mathsf{L}}^s, h_{\mathsf{T}}^s, h_{\mathsf{LT}}^s, h_{\mathsf{LS}}^s, h_{\mathsf{TS}}^s\}$, $\mathcal{Y}_h = \{\sigma_0^h, Q^h, b^h, \mathcal{H}_s^h, \mathcal{H}_{tw}^h, h_{\mathsf{L}}^h, h_{\mathsf{T}}^h, h_{\mathsf{LT}}^h, h_{\mathsf{LS}}^h, h_{\mathsf{TS}}^h\}$, $\mathcal{Y}_{tw}^{\text{hard}} = \{\sigma_0^{tw}, Q^{tw}, b^{tw}, \mathcal{H}_s^{tw}, \mathcal{H}_h^{tw}\}$, and $\mathcal{Y}_{tw}^{\text{yield}} = \{C_{\mathsf{LT}}^{tw}, C_{\mathsf{LS}}^{tw}, C_{\mathsf{T}}^{tw}, C_{\mathsf{TS}}^{tw}, C_{\mathsf{S}}^{tw}, C_{\mathsf{LT}}^{tw}, C_{\mathsf{LS}}^{tw}, C_{\mathsf{TS}}^{tw}, k\}$. These parameters are calibrated by minimizing the objective functions that include the yield stresses and lateral strain (Lankford) ratios along the material principal and off-axis directions. Detailed expressions for the objective functions and constraint conditions together with the calibration against crystal plasticity (CP) simulations are collated in *Supplementary Material* and a broad outline of the parameter calibration algorithm is presented in Appendix B. In the calibration process, we choose L-tension as the reference direction. This choice is not unique but a matter of convenience. The resulting expressions are consolidated in *Supplementary Material*, see Table S1 and Table S2. Table 1 consolidates the calibrated material parameters corresponding to the crystal plasticity results in Fig. 1. We note here that the keywords *soft* and *hard* respectively reflect the *basal* and *non-basal* modes of plasticity in HCP materials. However, we did not constrain their yield stresses to be in any particular order. With L-tension as the reference direction the calibration protocol gives $\sigma_0^h < \sigma_0^s$, which may appear to be at odds with the *hard* versus *soft* notion. However, it merely reflects that the hard glide governs the response while soft glide plays a secondary role, consistent with the CP results in Fig. 1(e).

4. Validation of the MSM

A detailed discussion of the calibrated MSM results is presented in the Section S2 of the *Supplementary Material*. As shown there, the trends captured by the MSM corroborate well with the CP results and the computational efficiency is high given that the MSM calibrations are performed using a single finite element.

In this section, we present several examples to demonstrate the validity of the calibrated MSM under uniaxial, biaxial and simple shear loading along general material directions. The results are compared against full-field crystal plasticity simulations for which the computational setup is the same as in Fig. 1(a). As in the calibration exercise, the crystal plasticity simulations are computationally expensive with nearly 90,000 3D (C3D4) finite elements. In contrast, the MSM predictions are based on a single 3D (C3D8) finite element calculation. We assume isotropic elasticity, with Young's modulus, $E = 43$ GPa and Poisson's ratio, $\nu = 0.29$. Quasi-static loading condition is considered with a nominal strain-rate $\dot{\varepsilon}^{nom} = 1 \times 10^{-3}$ s^{-1}. The strain rate sensitivity parameters for the three modes is taken to be $m^s = m^h = m^{tw} = 0.02$. The linear interpolation parameter, $\beta = 0.90$ (Appendix A) is used in all the cases.

Off-axis uniaxial loading:

First, we consider the off-axis responses of the polycrystal magnesium alloy loaded along directions that are at different angles to the principal material directions, cf. Indurkar et al. (2020). Two sets of loading orientations are considered (shown as insets in

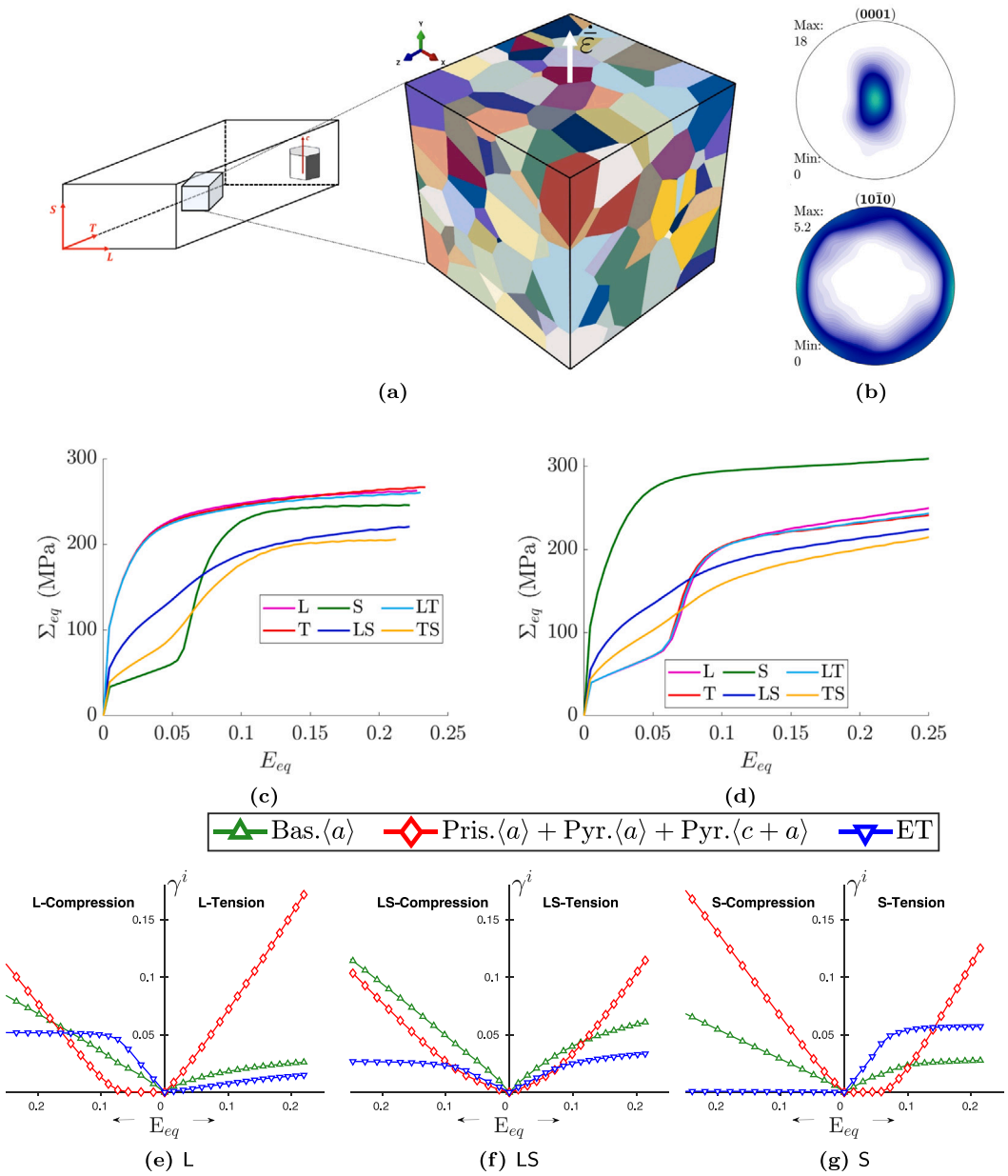

Fig. 1. (a) Polycrystal domain with material directions (L, T, S) and the global directions (x, y, z) and (b) (0001) and (10$\bar{1}$0) pole figures. Uniaxial stress–strain responses from crystal plasticity (CP) simulations in (c) tension and (d) compression for the texture in panel (b). Panels (e-g) illustrate the cumulative plastic shear strain evolution trends corresponding to soft glide (basal), hard glide (prismatic + pyramidal $\langle a \rangle$ + pyramidal $\langle c+a \rangle$, and extension twinning (ET)) for loading along L (panel (e)), LS (panel (f)), and S (panel (g)).
Source: Adapted from Indurkar et al. (2020).

Fig. 2(a) and Fig. 2(b)): θ_T–the angle made by the loading (y-) axis with the L direction in the LS plane, and θ_L–the angle made by the loading axis with the T direction in the TS plane. An appropriate rotation matrix is provided as input in ABAQUS® using the material orientation option, *ORIENT to align the particular direction in the material coordinate system with the global coordinate system.

As shown in Fig. 2, the MSM predicts well the uniaxial tensile and compressive flow stresses at different strain levels over the ranges of θ_T (Fig. 2(a)) and θ_L (Fig. 2(b)). In comparison, while the MSM predictions of the lateral deformation anisotropy ratios for the range of θ_T values is reasonable (Fig. 2(c)), there is some discrepancy for certain θ_L values (Fig. 2(d)). This discrepancy arises from the auxetic effect, which is captured by the crystal plasticity model (Indurkar et al., 2020) but not by the current MSM. In crystal plasticity, multiple deformation mechanisms with different hardening rates may produce similar macroscopic stresses

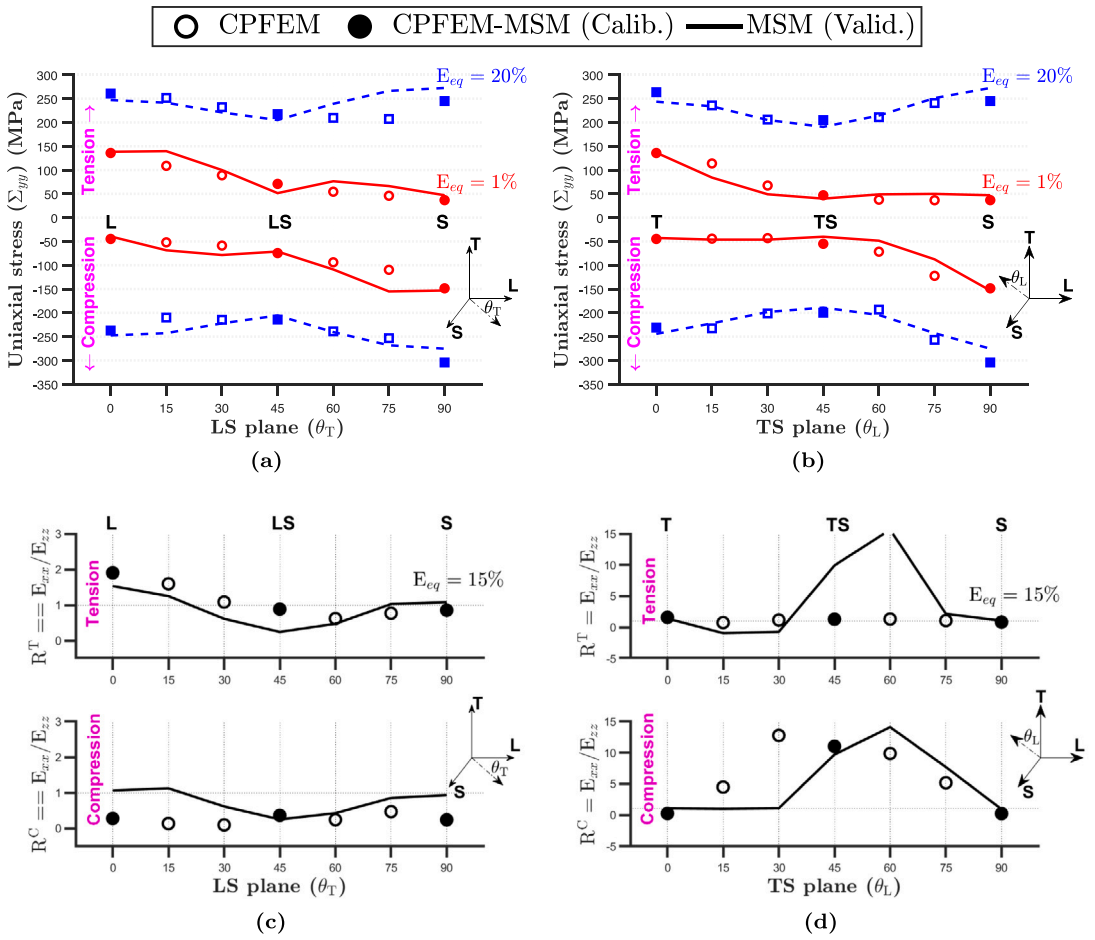

Fig. 2. Comparison of MSM results (solid or dashed lines) with crystal plasticity simulations (symbols) of Indurkar et al. (2020). Plastic anisotropy and tension–compression asymmetry at different strain levels along the LS (panel (a)) and TS planes (panel (b)). Panels (c) and (d) respectively show Lankford ratios in these planes.

but very different macroscopic lateral deformations, e.g. TS-tension versus TS-compression. In comparison, the HILL model, which is operative in this regime of deformation is agnostic to such finer details. More sophisticated anisotropic yield models (Barlat et al., 1991; Bron and Besson, 2004) or improved hardening models could remedy such special situations albeit with more fitting parameters.

Fig. 3 illustrates the full tensile (Fig. 3(a), 3(b)) and compressive (Fig. 3(c), 3(d)) stress–strain responses, and the corresponding mechanism strains ($\bar{\varepsilon}^{\alpha}$, α = soft glide, hard glide, twinning) for two θ_T and θ_L values. Comparing the tensile responses for $\theta_T = 15°$ and 30°, the role of the soft glide in the latter is obvious, which translates to an overall softer stress–strain behavior compared to the former. In the compressive responses, the orientation effect on the interaction between twinning and glide mechanisms is emphasized. These observations are consistent with the full-field crystal plasticity simulations (Indurkar et al., 2020).

Equibiaxial compression

Next, we examine the validity of MSM under equibiaxial compression in the LT and LS planes. In the crystal plasticity setting, equibiaxial loading is applied to the polycrystal (Fig. 1(a)) by prescribing a constant velocity in the global x (i.e., material L) and y (i.e., material T or S) directions using linear springs and adding a set of multi-point constraint equations such that the resulting macroscopic stress is $\boldsymbol{\Sigma} = \Sigma_{xx}\left(\mathbf{e}_x \otimes \mathbf{e}_x\right) + \Sigma_{yy}\left(\mathbf{e}_y \otimes \mathbf{e}_y\right)$ with $\Sigma_{xx} = \Sigma_{yy}$.

As seen from Figs. 4(a) and 4(b), the MSM predictions corroborate reasonably with the crystal plasticity results. The LT loading is initially governed by twinning deformation that saturates and is supplanted by the hard mode, which includes prismatic, pyramidal $\langle c \rangle$, and pyramidal $\langle c+a \rangle$ slip, cf. Fig. 4(b). This reflects in the sigmoidal stress–strain response, cf. Fig. 4(a). Under LS loading, the hard mode carries the plastic deformation, which compares very well with the crystal plasticity result. The corresponding evolution of the three yield surfaces under both loading orientations (Fig. 4(c)) reflect these observations.

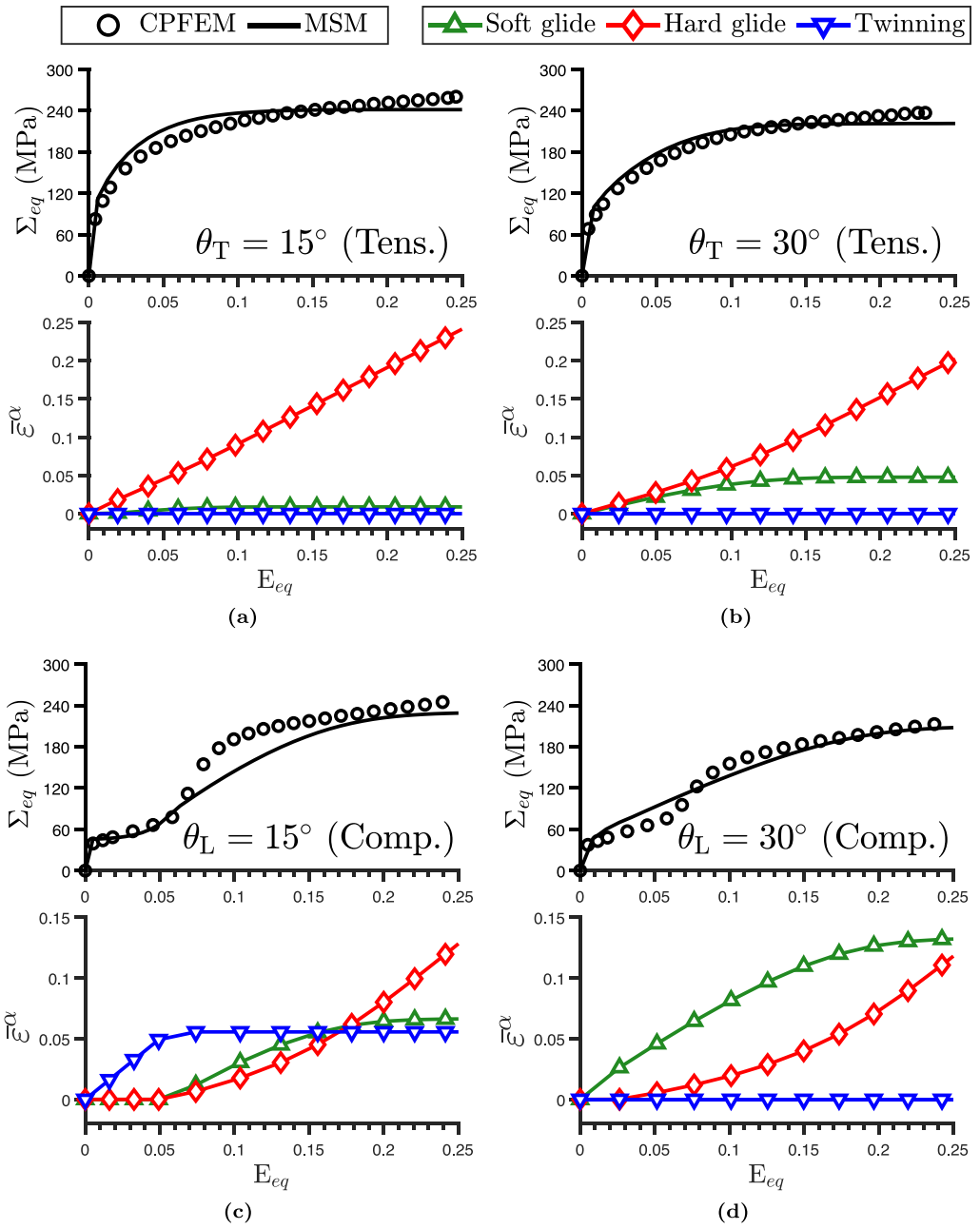

Fig. 3. MSM prediction (solid lines) against crystal plasticity (symbols) for particular values of θ_T and θ_L. Panels (a,b) compare equivalent stress–strain responses in tension (top row) and the mechanism strains ($\bar{\varepsilon}^\alpha$) predicted by MSM. Panels (c,d) compare equivalent stress–strain responses in compression (top row) and the mechanism strains ($\bar{\varepsilon}^\alpha$) predicted by MSM.

Simple shear

Finally, we demonstrate the efficacy of the MSM under shear loading. To that end, crystal plasticity simulations are conducted on the polycrystal with simple shear deformation applied in the LT and TS planes. For both simulations, nodes at the bottom LS plane are pinned. Simple shear simulation along LT is conducted by applying a constant velocity along the top LS plane in the L direction. Similarly, simple shear along TS is conducted by applying a shearing velocity along the top LS plane in the S direction.

Figs. 5(a) and 5(b) respectively show the $\Sigma_{eq} - E_{eq}$ and the accumulated mechanism shear strains. The comparison between the crystal plasticity and MSM simulations is encouraging for both the loading conditions. The stronger response of LT loading is due to the dominant hard mode. On the other hand, the TS response is weaker but with persistent hardening that emerges from the

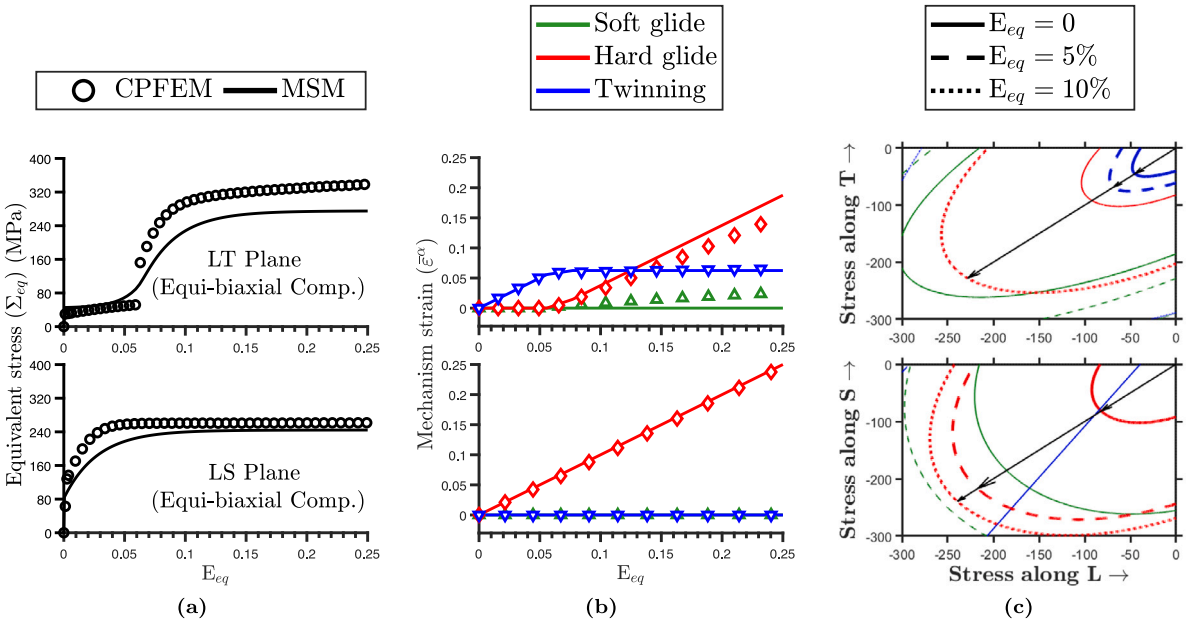

Fig. 4. (a,b) Comparison of MSM (solid lines) against crystal plasticity simulations (symbols) for equibiaxial compressive loading in the LT (top row) and LS (bottom row) planes. Panel (c) shows the evolution of the MSM yield surfaces in the LT and LS planes.

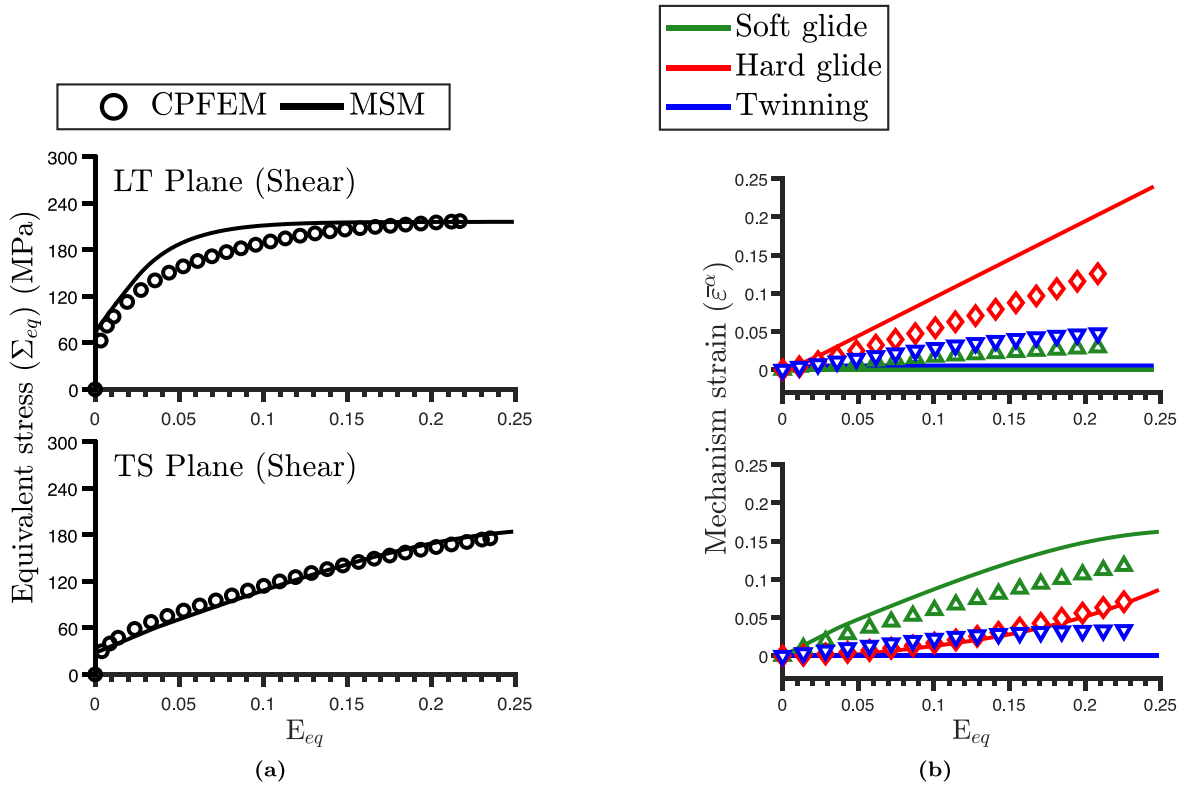

Fig. 5. Validation of MSM (solid lines) against crystal plasticity (symbols) for simple shear loading in the LT and LS planes.

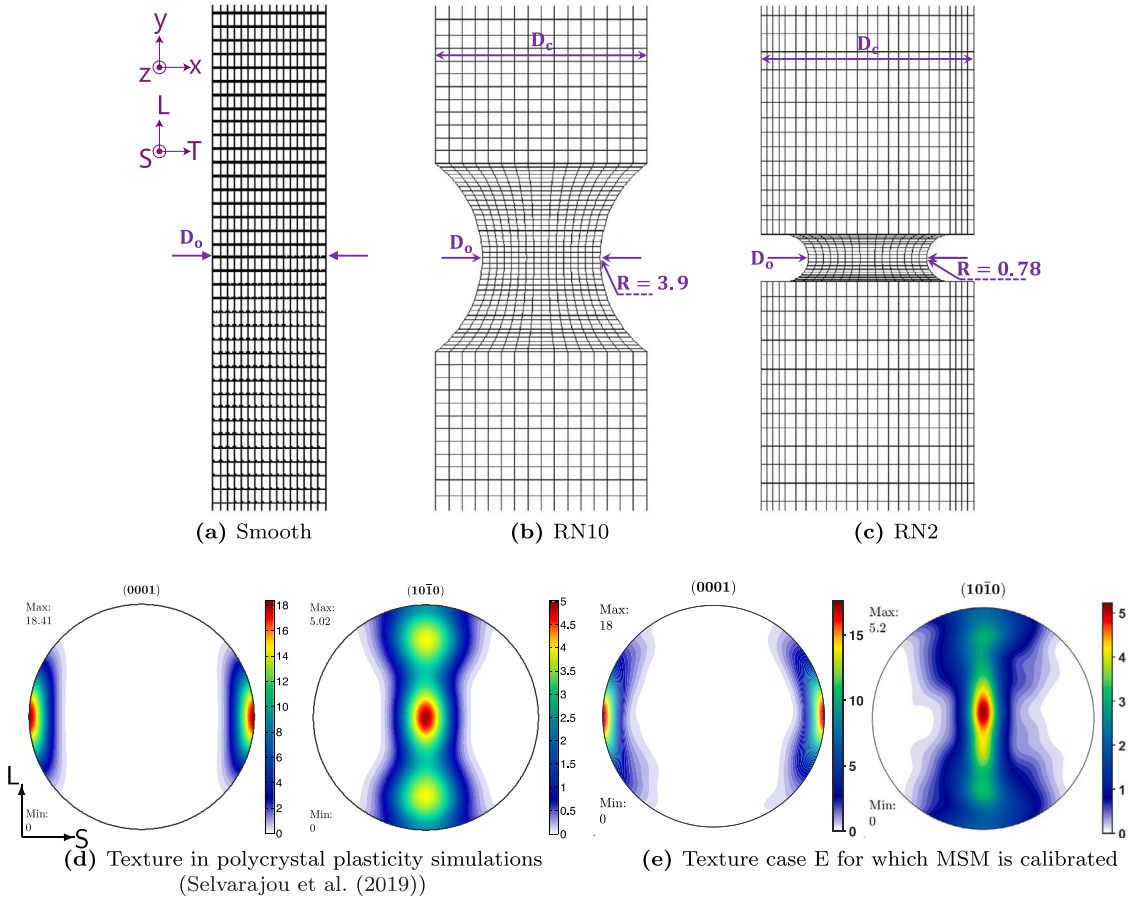

Fig. 6. Finite element geometries for (a) smooth, and (b) RN10, and (c) RN2 notched specimens. Panels (d) and (e) show the (0001) and (10$\bar{1}$0) pole figures of the texture employed for the CP simulations (Selvarajou et al., 2017) and the one for which the MSM material data set was calibrated.

dominant soft mode supported by the hard mode (crystal plasticity simulations indicate dominant pyramidal $\langle c + a \rangle$ slip) at later stages of deformation. Both the scenarios reveal lower extension twinning activity in the MSM compared to the crystal plasticity, which is compensated somewhat by the soft plasticity mode.

5. Application to boundary value problems

In the preceding section, the MSM was applied to a series of material point calculations, which are essentially single element calculations using the developed MSM-UMAT. As shown there, the MSM calculations corroborate very well with the high-resolution crystal plasticity simulations while also being computationally inexpensive. In this section, we demonstrate the efficacy of the MSM for larger scale calculations by choosing two sets of problems set at two different length-scales: (i) at the macroscopic scale: round bar specimens with different notch acuity subjected to nominally uniaxial tensile loading, and (ii) at the micromechanical scale: unit cell simulations of void growth and coalescence under prescribed triaxial stress states, typically occurring in notched bar geometries.

Round bar specimens

Fig. 6 shows three round-bar (smooth, RN10, and RN2) geometries subjected to nominally uniaxial tension. These geometries are identical to the experiments on rolled AZ31 Mg alloys (Kondori and Benzerga, 2014) loaded along the rolling (L) direction. The *ORIENT feature in ABAQUS/STANDARD® is used so that the material L direction is aligned with the global y-axis (loading direction) and the material in-plane transverse (T) and normal-to-rolling plane (S) directions are respectively aligned with the global x and z axes. At the top surface, a constant displacement rate ($\dot{U}_y$) is applied while the x-displacement is unconstrained. At the bottom surface, the y-displacement is constrained at all nodes while the x-displacement at the central node is fixed to avoid rigid rotation. The nominal strain rate $\dot{U}_y/L_0 = 1\times10^{-3}$ s^{-1} where L_0 is the original length of the specimen. In the figure, $D_c = 7$ mm and $D_0 = 3.9$ mm. The notch radii are also shown. The smooth, RN10 and RN2 are respectively discretized into $\sim 20,000$, 23,000, and 29,000 eight-node hexahedral finite elements with reduced integration (C3D8R in ABAQUS/STANDARD®) (see Fig. 6). The

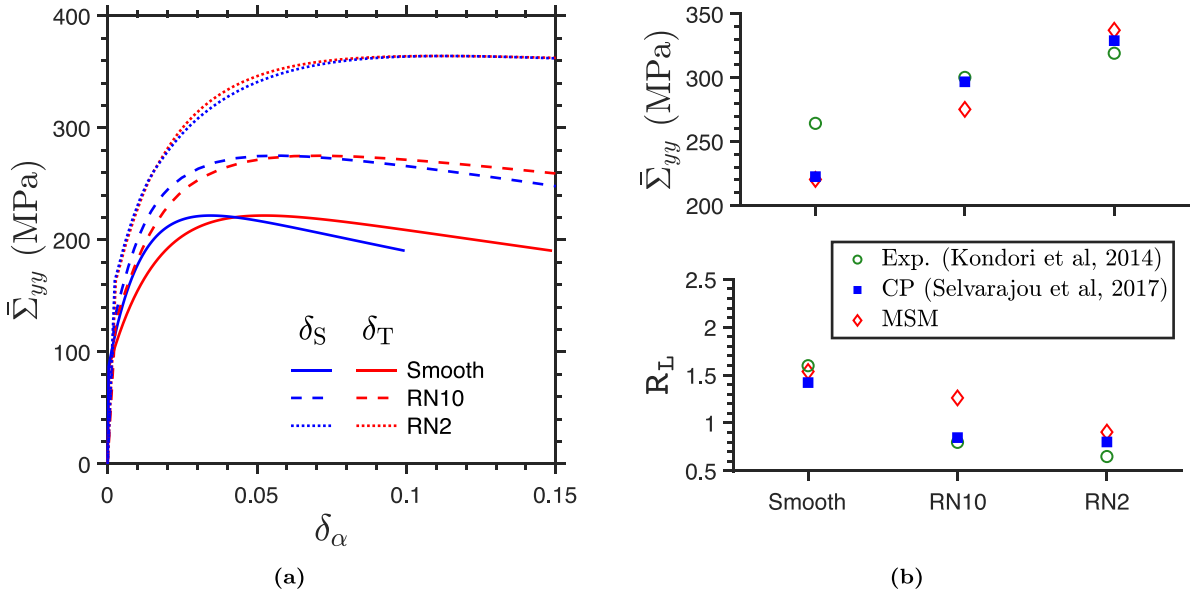

Fig. 7. (a) $\bar{\Sigma}_{yy} - \delta_\alpha$ in the T (blue) and S (red) directions. Panel (b) compares the MSM trends for $\bar{\Sigma}_{\text{peak}}$ and R_L with experiments and crystal plasticity results. The latter are reported at strains corresponding failure strains in experiments.

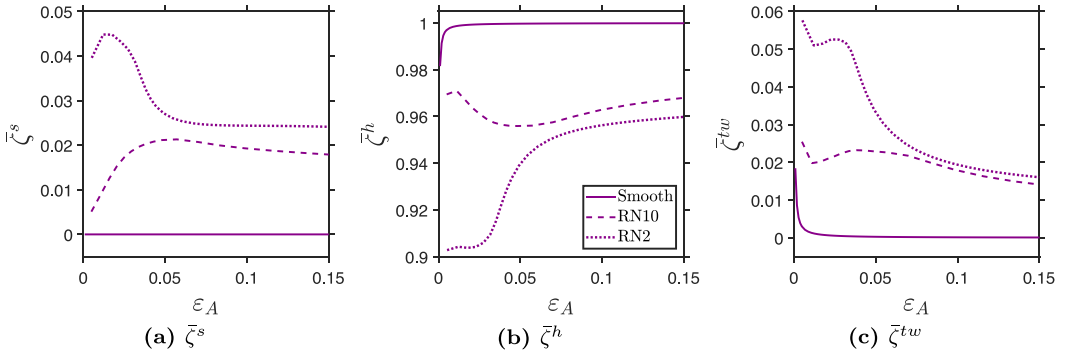

Fig. 8. Evolution of the volume averaged relative activities for (a) soft plasticity ($\bar{\zeta}^s$), (b) hard plasticity $\bar{\zeta}^h$, and (c) twinning plasticity ($\bar{\zeta}^{tw}$).

macroscopic responses are expressed in terms of the normalized force ($\bar{\Sigma}_{yy} = (F/A_0)$) and the normalized diametric reduction ($\delta_\alpha = \Delta D_\alpha / D_0$) where F is the total force along the loading direction, $A_0 = (\pi/4)D_0^2$, ΔD_α is the diametrical reduction along direction α (= T or S). The magnitude of the total areal strain is $\varepsilon_A = |\varepsilon_T| + |\varepsilon_S|$ where $\varepsilon_\alpha = \ln(D_\alpha/D_0)$ is the logarithmic strain along a lateral direction α. The strain anisotropy ratio is defined as $R_L = \varepsilon_T/\varepsilon_S$.

As seen from Fig. 7(a), increasing notch acuity (higher stress triaxiality) results in a higher peak normalized force and a delayed softening, which is consistent with the experiments (Kondori and Benzerga, 2014) and full-field crystal plasticity simulations (Selvarajou et al., 2017). Fig. 7(b) shows a reasonable comparison for the peak normalized force ($\bar{\Sigma}_{\text{peak}}$) and lateral strain anisotropy ratio (R_L) (measured at failure by Kondori and Benzerga (2014)) with the experiments and crystal plasticity simulations.

Defining the volume-averaged relative activity of the $i^{\text{th}}(= s, h, tw)$ mode:

$$\bar{\zeta}^i = \frac{\int \dot{\varepsilon}^i \mathrm{d}V}{\int \sum_{\alpha=1}^{3} \dot{\varepsilon}^\alpha \mathrm{d}V} \tag{11}$$

Fig. 8(a)–8(c) shows its evolution for the three specimens. Notably, the extension twinning activity is higher in the notched specimens, which results from the lateral tensile stresses, which is consistent with crystal plasticity simulations (Selvarajou et al., 2017). The drop in $\bar{\zeta}^{tw}$ (Fig. 8(c)) mimics the physical process of twinning induced reorientation by way of evolution of the twinning yield surface, thereby activating other plasticity modes. Further, the soft plasticity ($\bar{\zeta}^s$) also increases with increasing notch acuity. The activation of these additional mechanisms in the notched specimens leads to extra hardening, which is responsible for the higher $\bar{\Sigma}_{\text{peak}}$. Fig. 9(a)–9(b) and Fig. 9(c)–9(d) respectively reveal the lateral stress distributions predicted by the MSM. While a direct comparison of these distributions with full-field polycrystal notched bars simulations is difficult, we note that the qualitative

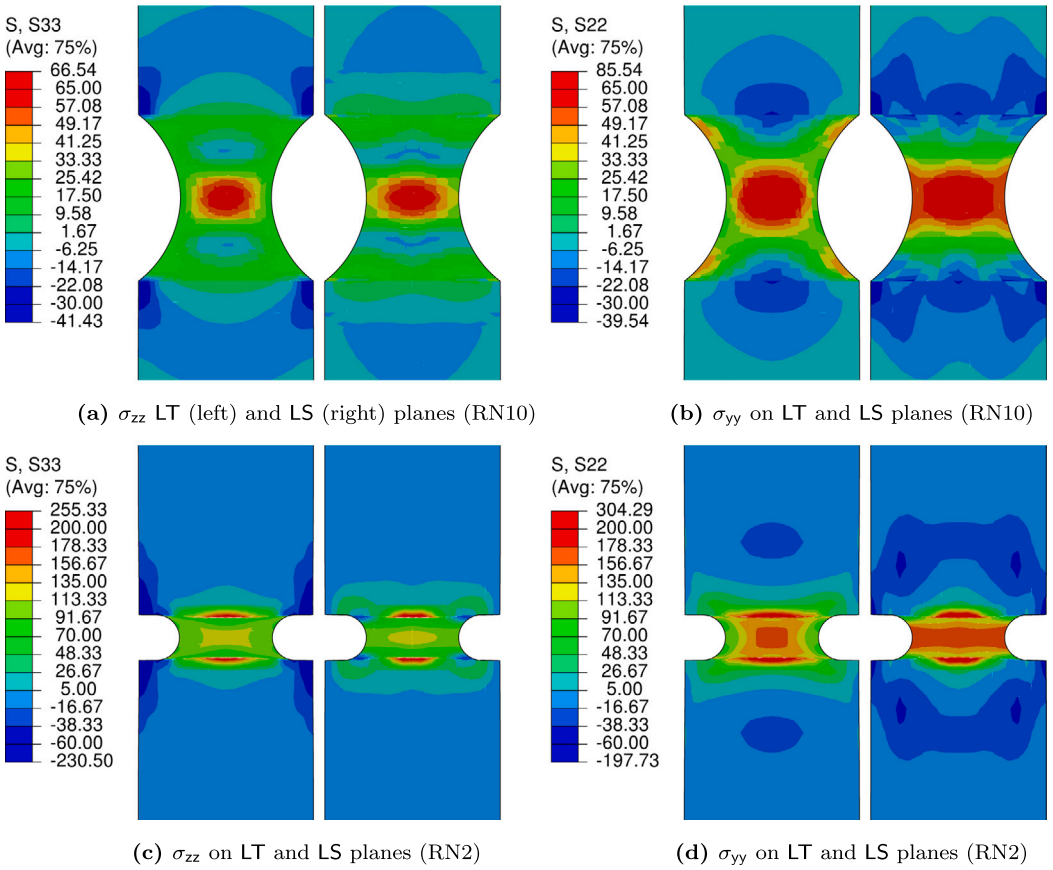

(a) σ_{zz} LT (left) and LS (right) planes (RN10) **(b)** σ_{yy} on LT and LS planes (RN10)

(c) σ_{zz} on LT and LS planes (RN2) **(d)** σ_{yy} on LT and LS planes (RN2)

Fig. 9. Lateral normal stresses (at $\epsilon_A = 0.1$) along T and S for (a,b) RN10 and (c,d) RN2 specimens. The contours are plotted in the LT (left sub-figures) and LS (right sub-figures) planes.

and quantitative trends compare reasonably well with the single crystal results, which is a limiting scenario of a textured material (see Fig. 8 in Selvarajou et al. (2016)).

Micromechanical scale: Unit cell simulation of void growth

Finally, we assess the MSM for a computationally intensive micromechanical problem of void growth under 3D tensile stress states. The motivation stems from recent unit cell studies conducted using CP on Mg single crystals (Selvarajou et al., 2019). We model a unit cell with an embedded spherical void at the center, Fig. 10, subjected to a constant stress triaxiality ratio ($\mathcal{T} = \Sigma_m/\Sigma_{eq}$) where Σ_m and Σ_{eq} are the macroscopic mean and von Mises equivalent stresses respectively. A 1/8th cell with symmetry boundary conditions is modeled to reduce computational expense; the details of loading implementation can be found in Selvarajou et al. (2019). The macroscopic stresses $\Sigma_{xx} = \Sigma_{zz}$ with Σ_{yy} being the primary stress; The initial lengths along the x-, y- and z-directions are $L_{x0} = L_{y0} = L_{z0} = L_0$. The primary loading is along the y-axis, which is aligned with the material L-direction while lateral T- and S- directions are aligned along x and z respectively. This situation is similar to the limiting case of a porous single crystal unit cell where the primary loading direction aligned along the prismatic $\langle a \rangle$-axis, cf. Selvarajou et al. (2019), save for texture effect. The macroscopic logarithmic strains are $E_{ii} = \ln(L_i/L_0)$ $(i = x, y, z$; no sum). The initial porosity $f_0 = (4\pi r_0^3/3L_0^3) = 0.01$. The current unit cell lengths are L_x, L_y and L_z and the void radii are r_x, r_y and r_z, and the current void aspect ratio and lateral ligament parameter are, respectively, $W_i = r_y/r_i$ and $\chi_i = 2r_i/L_i$ $(i = x, z)$.

Fig. 11 shows the macroscopic responses of the porous unit cell for $1/3 \leq \mathcal{T} \leq 3$. As expected, the peak stress and onset of coalescence (marked by x indicating the transition of from triaxial to uniaxial straining cf. Koplik and Needleman (1988)) decrease with increasing $\mathcal{T}$, Fig. 11(a). The uniaxial ($\mathcal{T} = 1/3$) response of the porous cell is nearly identical to the pristine (no void) unit cell case, which is a result of the lack of void growth, cf. Fig. 11(b). With increasing $\mathcal{T}$ the porosity grows exponentially, Fig. 11(b). In Fig. 11(c), the anisotropy of the lateral cell strains (E_{xx} and E_{zz}) is seen. At a given E_{yy}, $E_{xx} > E_{zz}$ for all levels of $\mathcal{T}$. Moreover, at high $\mathcal{T}$ levels ($\gtrsim 2$) the cell exhibits positive lateral straining along the z direction. These features are qualitatively consistent with the single crystal porous unit cell calculations of Selvarajou et al. (2019).

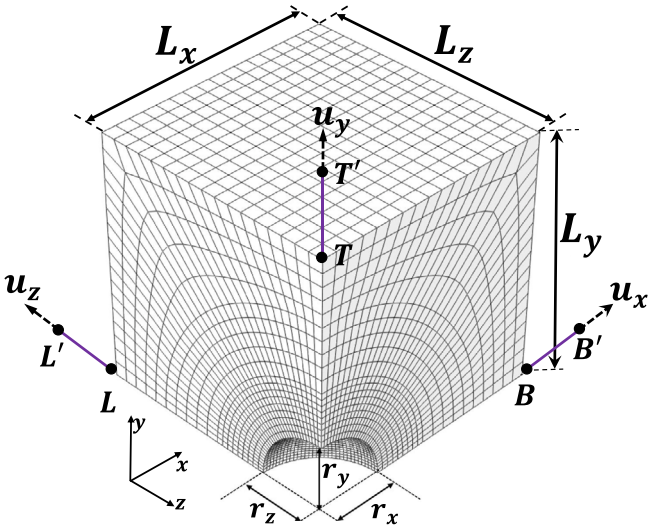

Fig. 10. Micromechanics of void growth. A $(1/8)^{th}$ portion of the voided unit cell is shown with the finite element discretization. The top, left and back faces of the unit cell are shown with elastic springs that are used to subject the unit cell to a state of constant stress triaxiality.

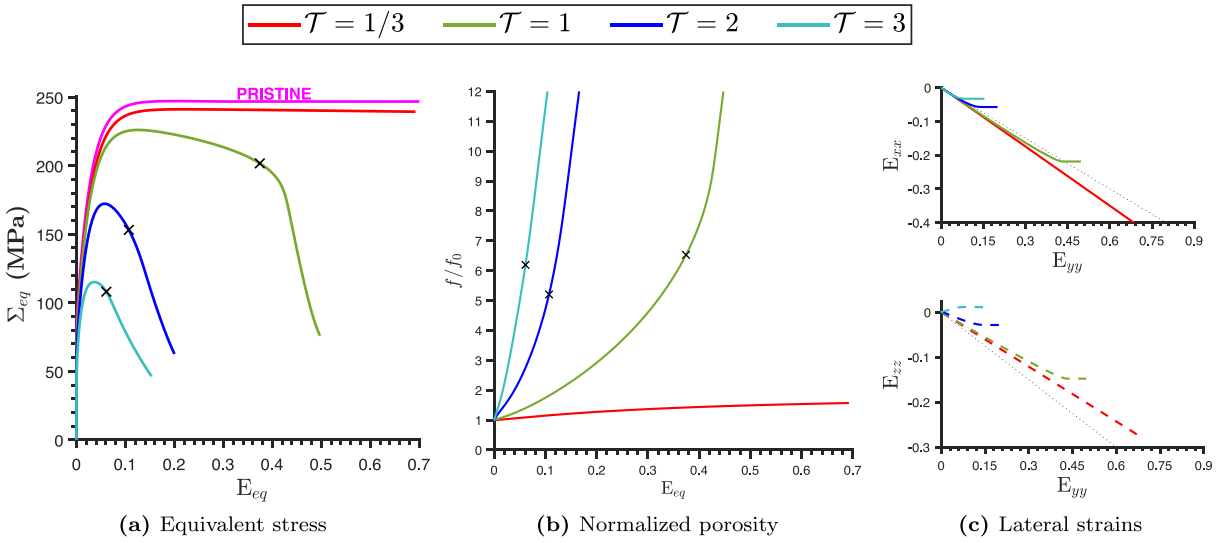

(a) Equivalent stress **(b)** Normalized porosity **(c)** Lateral strains

Fig. 11. Spherically voided unit cell $(f_0 = 0.01)$ subjected to constant stress triaxiality levels ($\mathcal{T} = 1/3, 1, 2$ and 3). The maximum principal stress is along L: (a) $\Sigma_{eq} - E_{eq}$ response; x denotes onset of coalescence, (b) Normalized porosity evolution, and (c) Evolution of lateral cell strains, E_{xx} and E_{zz}; the dotted lines indicate the response for an isotropic J_2 material.

Fig. 12 shows the trends for the critical strain at the onset of coalescence, (E_{cr}) (Fig. 12(a)), and the corresponding critical porosity at the onset (Fig. 12(b)), critical void aspect ratio anisotropy (Fig. 12(c)) and critical ligament ratio anisotropy (Fig. 12(d)). Similar results for pure Mg porous single crystal from Selvarajou et al. (2019) are included for reference. A direct comparison between the crystal plasticity and MSM is not the aim of these plots as the former is significantly more plastically anisotropic, while the net plastic anisotropy is much tempered in the polycrystal to which the MSM is calibrated. Another aspect is that in the single crystal unit cell calculations, the formation of twin sector boundaries around the void is observed, which affect the evolution of void geometry. Such an effect is not directly incorporated in an MSM simulation. We note that the differences do not reflect the limitation of the MSM but rather points to the potential deviations in the porous material response brought about by polycrystal texturing.

Fig. 13(a)–13(c) collate the volume averaged relative activity evolution ($\bar{\zeta}^i$, Eq. (11)) predicted by the MSM as a function of $\mathcal{T}$. For comparison, trends from single crystal plasticity simulations of voided pure Mg unit cell (Selvarajou et al., 2019) are shown in Figs. 13(d)–13(f). Finer details aside, the trends for each set of mechanism in the MSM results corroborate well with those in

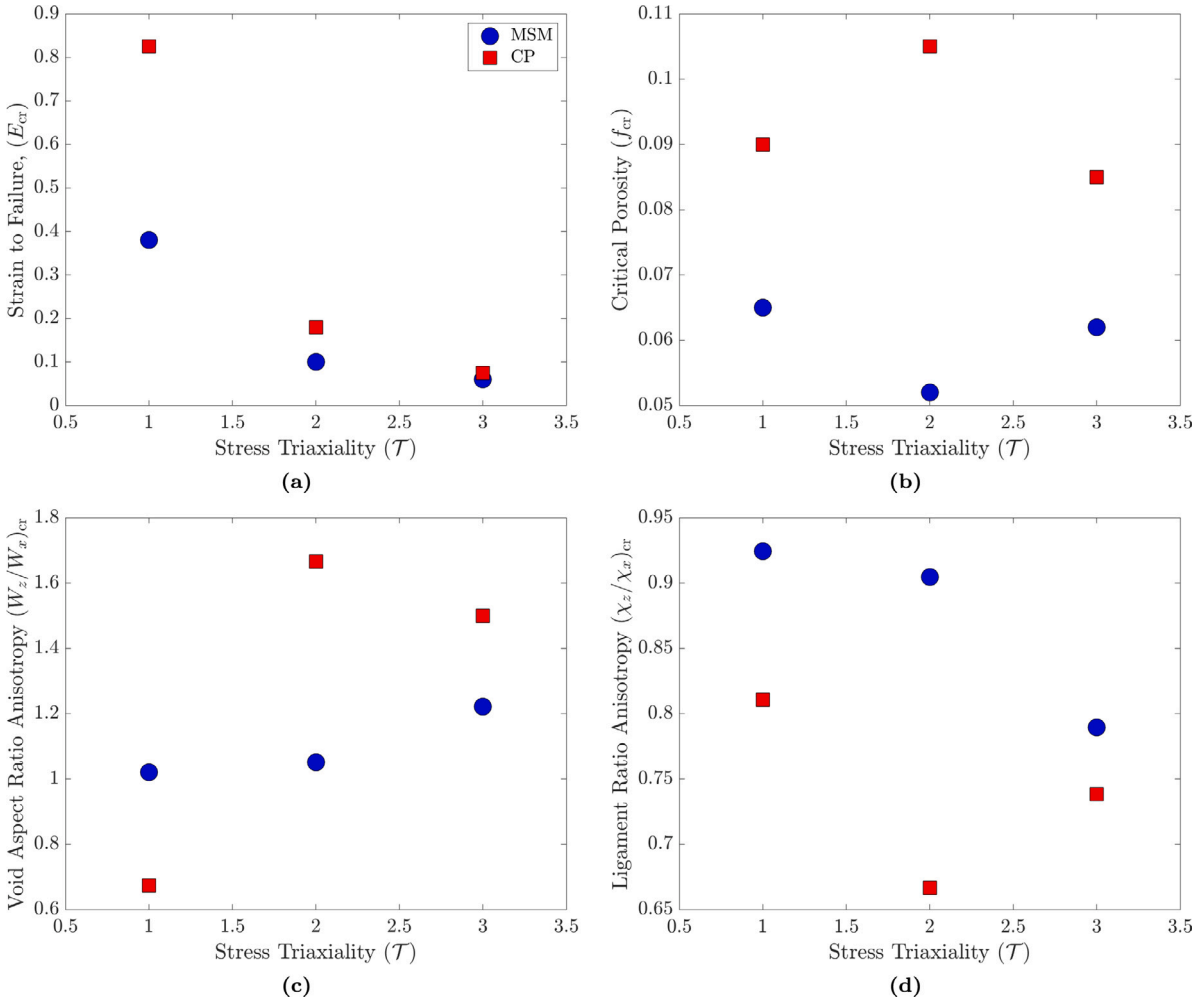

Fig. 12. MSM predictions (circles) of critical values corresponding to the onset of failure (a) equivalent strain (E_c), (b) porosity (f_c), (c) relative void aspect ratio anisotropy ($(W_z/W_x)_c$), and (d) Ligament parameter anisotropy ($(\chi_z/\chi_x)_c$). The trends are compared against single crystal predictions of Selvarajou et al. (2019) shown by square symbols.

the crystal plasticity results. For instance, note the strong dependence of the soft slip (correspondingly, the basal slip in crystal plasticity) on $\mathcal{T}$. Similarly, MSM predicts a stronger contribution from twinning with increasing triaxiality, which is consistent with the results of Selvarajou et al. (2019).

Fig. 14 shows a collage of the mechanism strain distributions at the onset of coalescence for different triaxiality levels, save for $\mathcal{T} = 1/3$ where no coalescence is predicted (distribution plotted for $E_{eq} = 0.6$). The simulations predict distinct domains around the void where each mechanism prevails. The soft glide is dominant in the LS-plane but also emerges in the plane of coalescence (i.e., TS plane) at high triaxiality levels, Fig. 14(a)–14(c). In contrast, twinning (Fig. 14(d)–14(f)) is concentrated in the polar region of the void at low to moderate triaxiality levels ($1/3 \lesssim \mathcal{T} \lesssim 1$) but occupies a substantial portion of the LT plane at $\mathcal{T} = 3$. Finally, the hard glide (Fig. 14(g)–14(i)) persists in all three planes but is concentrated in the immediate neighborhood of the void. It also governs the preferential strain localization in the T direction. These trends corroborate with the high resolution crystal plasticity simulations (Selvarajou et al., 2019).

6. Summary

We present a multi-surface model (MSM) of plasticity incorporating anisotropy and tension–compression asymmetry for HCP metals. Motivated by the importance of disparate nature of key deformation mechanisms in magnesium and its alloys — basal slip, non-basal slip, and extension twinning and their evolution, a three-surface representation is proposed. The model is computationally attractive compared to high-resolution single crystal plasticity while retaining for the main features of HCP deformation mechanisms in a physically relevant manner. Using a two-stage calibration strategy, the MSM constitutive parameters are calibrated to a synthetic

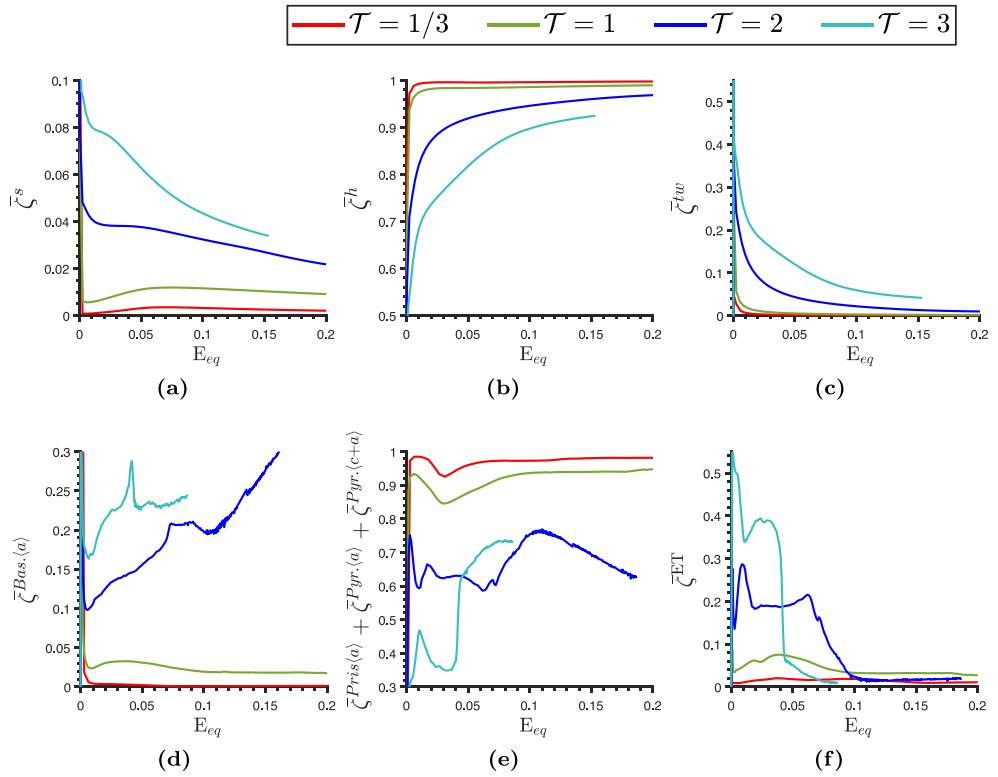

Fig. 13. (a-c) Triaxiality-dependent volume averaged relative activities ($\bar{\zeta}^i$) of different mechanisms as predicted by (a-c) MSM, and (d-f) pure Mg single crystal (adapted from Selvarajou et al. (2019)). The soft slip (a) in MSM is correlated with basal slip in crystal plasticity (d), hard slip (b) with the sum of prismatic, pyramidal $\langle a\rangle$ and pyramidal $\langle c+a\rangle$ slip (e), and twinning (c) with ET (f).

Table 2
A comparison of $\hat{t}$ and $\tilde{t}$ values for smooth and round notched specimens.

Geometry	$\hat{t}^{\text{SYS}}$	$\hat{t}^{\text{CPU}}$	$\tilde{t}^{\text{SYS}}$	$\tilde{t}^{\text{CPU}}$
Smooth	4.91	3.14	4.92	3.14
RN10	2.98	1.5	2.9	1.49
RN2	3.16	1.05	5.56	1.81

3D response dataset obtained from CP simulations representing a rolled polycrystalline Mg alloy. The MSM responses are validated against different crystal plasticity simulations for a range of loading orientations under uniaxial, equibiaxial, and simple shear states. Further, the MSM is assessed for a range of boundary value problems including smooth and round notched bars, as well as the micromechanics of void growth under controlled stress triaxiality.

We briefly comment on the computational efficacy of the MSM simulations compared to the CP simulations. For this purpose, the smooth and notched bar problems serve as a good basis as the mesh discretization and boundary conditions are identical for the CP and the MSM simulations. Both sets of simulations are conducted on the same computational cluster and using the same version of ABAQUS/STANDARD®. Let $\hat{t}^{\text{SYS}} = t^{\text{SYS}}_{\text{CP}}/t^{\text{SYS}}_{\text{MSM}}$ and $\hat{t}^{\text{CPU}} = t^{\text{CPU}}_{\text{CP}}/t^{\text{CPU}}_{\text{MSM}}$ where $t^{\text{SYS}}_{\text{CP}}$ and $t^{\text{SYS}}_{\text{MSM}}$ are respectively the system times taken per increment by a CP and its MSM counterpart, and $t^{\text{CPU}}_{\text{CP}}$ and $t^{\text{CPU}}_{\text{MSM}}$ the total CPU time taken per increment. The corresponding system time and total CPU time ratios taken per iteration are defined using $\tilde{t}^{\text{SYS}}$ and $\tilde{t}^{\text{CPU}}$. The information for the CP simulations is extracted from Selvarajou et al. (2017).

Table 2 highlights the computational efficiency of the MSM calculations. While these ratios may seem modest in some cases, the memory requirement of the MSM is much less compared to the CP, which is a significant advantage. The MSM computational cost comes from the need to calculate the effective stress expressions and flow vectors of the plasticity modes, which is not required in rate-dependent CP where the resolved shear stress calculation and explicit update of the Schmidt tensor is relatively less expensive. Moreover, the high anisotropy, particularly at small strains makes the soft glide and the twinning yield surfaces very skewed, which adds to the MSM computational time.

The efficacy of the MSM can be improved by optimizing the calculation of the effective stresses, flow vectors, and the mechanism strains especially when the different modes have very different contributions. Further improvement could be realized by replacing the current explicit update algorithm with a fully implicit stress update algorithm together with the consistent tangent modulus

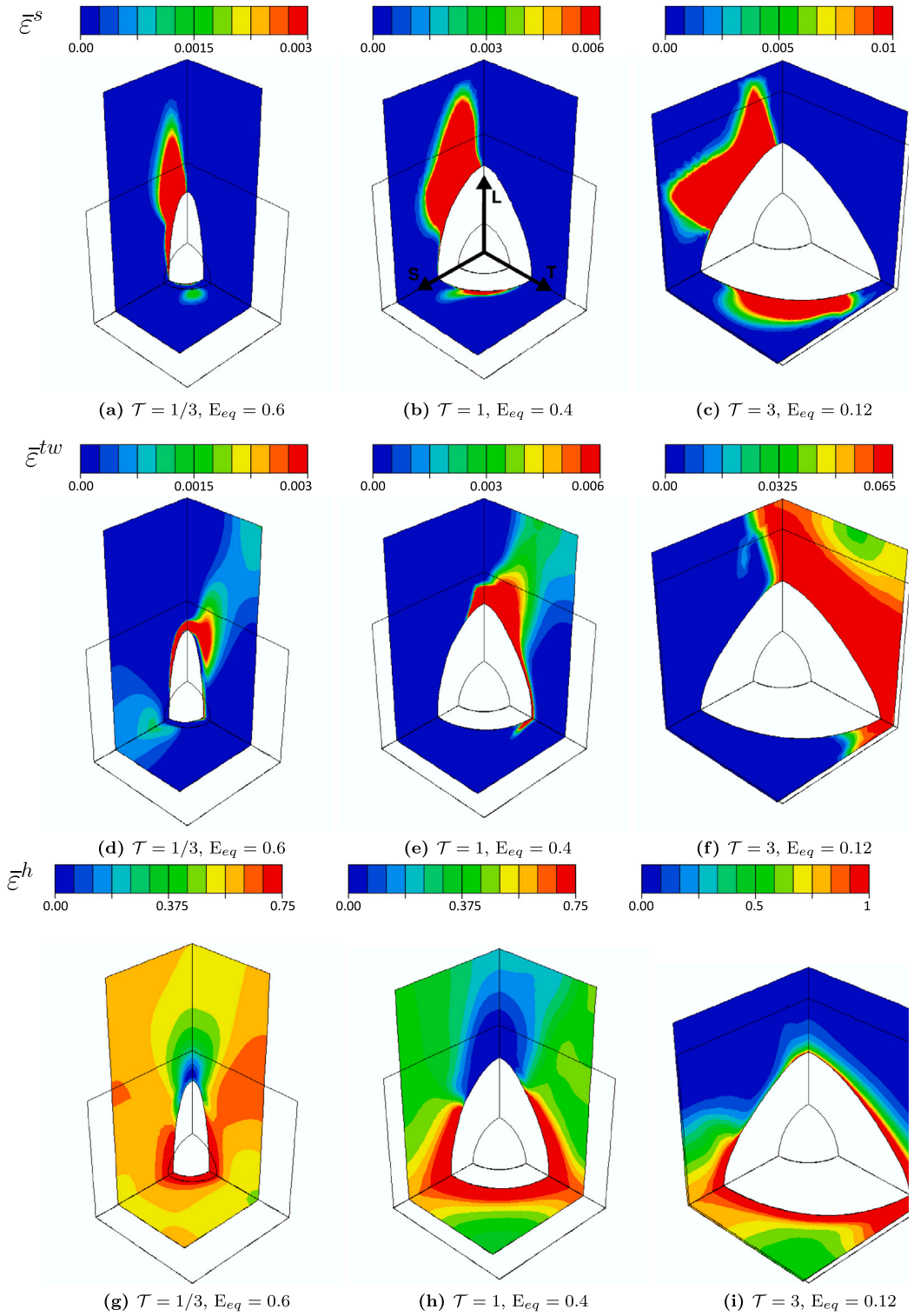

Fig. 14. Distributions of $\bar{\varepsilon}^s$ (a-c), $\bar{\varepsilon}^{tw}$ (d-f), and $\bar{\varepsilon}^h$ (g-h) around the void for $\mathcal{T} = 1/3, 1$ and 3. The contours correspond to onset of coalescence (except $\mathcal{T} = 1/3$).

calculation (Simo et al., 1988; Simo and Hughes, 2006). Although the fully implicit algorithm can be computationally demanding (as it requires calculating $\partial^2\bar{\sigma}/\partial\boldsymbol{\sigma}^2$), a faster convergence may be achieved. The MSM approach and its computational implementation can be adapted to accommodate other yield criteria and hardening rules than those implemented in this work.

CRediT authorship contribution statement

Padmeya P. Indurkar: Methodology, Software development, Formal analysis, Writing – original draft, Writing – review & editing. **Shailendra P. Joshi:** Conceptualization, Methodology, Formal analysis, Writing – original draft, Writing – review & editing, Supervision, Funding acquisition.

Declaration of competing interest

The authors declare that they have no known competing financial interests or personal relationships that could have appeared to influence the work reported in this paper.

Data availability

Data will be made available on request.

Acknowledgments

SPJ wishes Prof. Yonggang Huang on his 60^{th} birthday. SPJ acknowledges support provided by the National Science Foundation, United States under Grant Number CMMI-1932976 and by the Army Research Laboratory, United States under Cooperative Agreement Number W911NF-12-2-0022. The views and conclusions contained in this document are those of the authors and should not be interpreted as representing the official policies, either expressed or implied, of the Army Research Laboratory or the U.S. Government. The U.S. Government is authorized to reproduce and distribute reprints for Government purposes notwithstanding any copyright notation herein. PPI acknowledges support from NUS Research Scholarship. The authors acknowledge the use of the Opuntia Cluster and the advanced support from the Research Computing Data Core at the University of Houston to carry out the research presented here.

Appendix A. Computational implementation

In Eq. (2), each yield surface satisfies the normality rule. For details on obtaining the flow vectors (Eq. (2)) $\mathbf{p}^i = \partial\mathcal{F}^i/\partial\boldsymbol{\sigma}$ for ith mode ($i = s, h, tw$), the reader is referred to Indurkar (2020). The Jaumann stress rate is given by:

$$\dot{\boldsymbol{\sigma}}_J = \mathbb{L} : \mathbf{D} - \sum_i \dot{\bar{\varepsilon}}^i \mathbf{P}^i \qquad (i \in \{s, h, tw\}) \tag{A.1}$$

where $\mathbf{P}^i = \mathbb{L} : \mathbf{p}^i$. The effective stress rate, $\dot{\bar{\sigma}}^i$ (Eq. (4)) is $\dot{\bar{\sigma}}^i = \mathbf{p}^i : \dot{\boldsymbol{\sigma}}_J$. Defining $\tilde{P}^i_j = \mathbf{p}^i : \mathbf{P}^j$, Eq. (A.1) gives:

$$\dot{\bar{\sigma}}^i = \mathbf{p}^i : \mathbb{L} : \mathbf{D} - \sum_j \dot{\bar{\varepsilon}}^j \tilde{P}^i_j \tag{A.2}$$

From a numerical standpoint, over the time interval $\{t, t+\Delta t\}$ the incremental effective viscoplastic strain, $\Delta\bar{\varepsilon}_i$ for the ith mode as:

$$\Delta\bar{\varepsilon}^i = \Delta t \left[(1-\beta)\,\dot{\bar{\varepsilon}}^i_t + \beta\dot{\bar{\varepsilon}}^i_{t+\Delta t}\right] \tag{A.3}$$

where $0 \le \beta \le 1$ is an interpolation parameter; in this work, we set $\beta = 0.9$ (Peirce et al., 1984). Let $\dot{\bar{\varepsilon}}^i \equiv \left(\Delta\bar{\varepsilon}^i/\Delta t\right)$, then at $t+\Delta t$ the estimate for $\dot{\bar{\varepsilon}}^i_{t+\Delta t}$ is obtained using Taylor series. For example, with $i = s$:

$$\dot{\bar{\varepsilon}}^s_{t+\Delta t} = \dot{\bar{\varepsilon}}^s_t + \frac{\partial\dot{\bar{\varepsilon}}_s}{\partial\bar{\varepsilon}_s}\dot{\bar{\varepsilon}}^s\Delta t + \frac{\partial\dot{\bar{\varepsilon}}_s}{\partial\bar{\varepsilon}_h}\dot{\bar{\varepsilon}}^h\Delta t + \frac{\partial\dot{\bar{\varepsilon}}_s}{\partial\bar{\varepsilon}_{tw}}\dot{\bar{\varepsilon}}^{tw}\Delta t + \frac{\partial\dot{\bar{\varepsilon}}_s}{\partial\bar{\sigma}_s}\dot{\bar{\sigma}}^s\Delta t \tag{A.4}$$

which yields (upon substitution in Eq. (A.3) and dividing both sides by Δt),

$$\dot{\bar{\varepsilon}}^s = \dot{\bar{\varepsilon}}^s_t + \beta\Delta t\left(\frac{\partial\dot{\bar{\varepsilon}}_s}{\partial\bar{\varepsilon}_s}\dot{\bar{\varepsilon}}^s + \frac{\partial\dot{\bar{\varepsilon}}_s}{\partial\bar{\varepsilon}_h}\dot{\bar{\varepsilon}}^h + \frac{\partial\dot{\bar{\varepsilon}}_s}{\partial\bar{\varepsilon}_{tw}}\dot{\bar{\varepsilon}}^{tw} + \frac{\partial\dot{\bar{\varepsilon}}_s}{\partial\bar{\sigma}_s}\dot{\bar{\sigma}}^s\right) \tag{A.5}$$

Note that the above Taylor series expansion is written following Eq. (4) such that $\dot{\bar{\varepsilon}}^s$ is a function of $\bar{\varepsilon}^s$, $\bar{\varepsilon}^h$, $\bar{\varepsilon}^{tw}$ and $\bar{\sigma}^s$. Similar expressions can be obtained for the other two modes and thus, for a mode $i \in \{s, h, tw\}$ (see Indurkar, 2020 for details), we write:

$$\dot{\bar{\varepsilon}}^i\left[1+\xi^i\right] = (\dot{\bar{\varepsilon}}^i)_t + \frac{\xi^i}{\bar{H}^i_i}\left[\mathbf{Q}^i : \mathbf{D} - \sum_{j\neq i}\dot{\bar{\varepsilon}}^j\bar{H}^i_j\right] \qquad \text{(no sum on } i\text{)} \tag{A.6}$$

where

$$\bar{H}^i_j = \tilde{P}^i_j\left(\frac{\partial\dot{\bar{\varepsilon}}_i}{\partial\bar{\sigma}_j}\right)_{j=i} - \frac{\partial\dot{\bar{\varepsilon}}_i}{\partial\bar{\sigma}_j}; \qquad \mathbf{Q}^i = \left(\mathbf{p}^i : \mathbb{L}\right)\left(\frac{\partial\dot{\bar{\varepsilon}}_i}{\partial\bar{\sigma}_j}\right)_{j=i}; \qquad \xi^i = \beta\Delta t\left(\bar{H}^i_j\right)_{j=i} \qquad \text{(no sum on } i\text{)} \tag{A.7}$$

The resulting system of equations can be represented in the matrix form:

$$\underbrace{\begin{bmatrix}\dot{\bar{\varepsilon}}^s\\ \dot{\bar{\varepsilon}}^h\\ \dot{\bar{\varepsilon}}^{tw}\end{bmatrix}}_{[\mathcal{E}]} = \underbrace{\begin{bmatrix}\bar{H}^s_s\left(1+\xi^s\right) & \xi^s\bar{H}^s_h & \xi^s\bar{H}^s_{tw}\\ \xi^h\bar{H}^h_s & \bar{H}^h_h\left(1+\xi^h\right) & \xi^h\bar{H}^h_{tw}\\ \xi^{tw}\bar{H}^{tw}_s & \xi^{tw}\bar{H}^{tw}_h & \bar{H}^{tw}_{tw}\left(1+\xi^{tw}\right)\end{bmatrix}^{-1}}_{[\Lambda]} \underbrace{\begin{bmatrix}\bar{H}^s_s\dot{\bar{\varepsilon}}^s_t+\xi^s\left(\mathbf{Q}^s:\mathbf{D}\right)\\ \bar{H}^h_h\dot{\bar{\varepsilon}}^h_t+\xi^h\left(\mathbf{Q}^h:\mathbf{D}\right)\\ \bar{H}^{tw}_{tw}\dot{\bar{\varepsilon}}^{tw}_t+\xi^{tw}\left(\mathbf{Q}^{tw}:\mathbf{D}\right)\end{bmatrix}}_{[\mathcal{R}]} \tag{A.8}$$

Once $\mathcal{E}$ is calculated (i.e. the corrected rates of $\bar{\varepsilon}^i$), the stress update follows from Eq. (A.1). The flow vectors ($\mathbf{p}^i$) are updated to calculate the plastic rates of deformation for each mode ($\mathbf{D}^i_p$) using Eq. (2).

Substituting $\dot{\bar{\varepsilon}}^s$, $\dot{\bar{\varepsilon}}^h$ and $\dot{\bar{\varepsilon}}^{tw}$ from Eq. (A.8) in Eq. (A.2), we obtain:

$$\dot{\boldsymbol{\sigma}}_J = \underbrace{\mathbb{L}:\mathbf{D}}_{\substack{\text{Elastic}\\ \text{update}}} - \underbrace{\mathbf{P}^s\hat{\mathbf{\Lambda}}^s\mathcal{R}}_{\substack{\text{Soft glide}\\ \text{plastic corrector}}} - \underbrace{\mathbf{P}^h\hat{\mathbf{\Lambda}}^h\mathcal{R}}_{\substack{\text{Hard glide}\\ \text{plastic corrector}}} - \underbrace{\mathbf{P}^{tw}\hat{\mathbf{\Lambda}}^{tw}\mathcal{R}}_{\substack{\text{Twinning}\\ \text{plastic corrector}}} \tag{A.9}$$

where, $\hat{\mathbf{\Lambda}}^s = \begin{bmatrix}\Lambda^s_s & \Lambda^s_h & \Lambda^s_{tw}\end{bmatrix}$, $\hat{\mathbf{\Lambda}}^h = \begin{bmatrix}\Lambda^h_s & \Lambda^h_h & \Lambda^h_{tw}\end{bmatrix}$, $\hat{\mathbf{\Lambda}}^{tw} = \begin{bmatrix}\Lambda^{tw}_s & \Lambda^{tw}_h & \Lambda^{tw}_{tw}\end{bmatrix}$ are respectively the first, second, and the third row of $[\mathbf{\Lambda}]$ in Eq. (A.8). Segregating the terms which involve $\mathbf{D}$ from the plastic correctors, we obtain:

$$\dot{\boldsymbol{\sigma}}_J = \mathbb{L}^{\tan}:\mathbf{D} - \left(\mathbf{P}^s\hat{\mathbf{\Lambda}}^s + \mathbf{P}^h\hat{\mathbf{\Lambda}}^h + \mathbf{P}^{tw}\hat{\mathbf{\Lambda}}^{tw}\right)\begin{bmatrix}\bar{H}^s_s\dot{\bar{\varepsilon}}^s_t & \bar{H}^h_h\dot{\bar{\varepsilon}}^h_t & \bar{H}^{tw}_{tw}\dot{\bar{\varepsilon}}^{tw}_t\end{bmatrix}^{\mathrm{T}} \tag{A.10}$$

where the tangent modulus $\mathbb{L}^{\tan}$ is:

$$\mathbb{L}^{\tan} = \mathbb{L} - \sum_{i,j\,=\,s,h,tw}\sum \xi^j\Lambda^i_j\left(\mathbf{P}^i\otimes\mathbf{Q}^j\right) \tag{A.11}$$

Eq. (A.11) reduces to the one in Peirce et al. (1984) for the case of single yield surface.

The elastic ($\boldsymbol{\varepsilon}_e$) and the total plastic ($\boldsymbol{\varepsilon}_p$) strains are calculated as:

$$\boldsymbol{\varepsilon}_e = \int_0^t \mathbf{D}_e\,\mathrm{d}t \qquad \boldsymbol{\varepsilon}_p = \int_0^t\left(\mathbf{D}^s_p+\mathbf{D}^h_p+\mathbf{D}^{tw}_p\right)\mathrm{d}t \tag{A.12}$$

The computational implementation is verified for several simplified cases (including the degenerate cases of single surface models), which can be accessed. here[1]

Appendix B. MSM calibration protocol

The calibration protocol for the MSM requires setting up objective functions ($\mathcal{G}_i$) using the expressions for the mechanism-based flow stress and lateral deformation anisotropy (Lankford ratios) along the material principal (L,T,S) and off-principal (LT, LS, TS) axes. In the present model, the soft and hard modes of plasticity are symmetric in tension and compression whereas the twinning mode is asymmetric. In all, there are 24 objective functions: 6 direction × 2 loading states (tension, compression) × 2 variables (flow stress and Lankford ratio). A particular objective function, $\mathcal{G}_i$, is normalized by the maximum value, i.e., either $\left(\max\left(\sigma^{\mathrm{sim}}_{dir,state}\right)\right)^2$ or $\left(\max\left(\mathrm{R}^{\mathrm{sim}}_{dir,state}\right)\right)^2$, and is denoted hereafter by $\bar{\mathcal{G}}_i$. Details of these objective functions are given in Supplementary Material. Based on these objective functions, a constrained optimization problem is written as follows:

$$\text{Minimize}\;\; \mathsf{E} = \sum_{i=1}^{\mathcal{N}} w_i\bar{\mathcal{G}}_i,\;\text{such that}\;\mathcal{J}_i < 0\;\text{and}\;-1\le k\le 1 \tag{B.1}$$

where w_i are the weights (set equal to unity in the present work). Eq. (B.1) is subject to $\mathcal{M}(=22)$ non linear conditions, $\mathcal{J}_i < 0$, which involve a parameter set $\mathcal{Y}$ that includes all the material parameters of the MSM. The full parameter set to be calibrated is $\mathcal{Y} = \begin{bmatrix}\mathcal{Y}_s & \mathcal{Y}_h & \mathcal{Y}^{\mathrm{hardening}}_{tw} & \mathcal{Y}^{\mathrm{yielding}}_{tw}\end{bmatrix}$, where

$$\mathcal{Y}_s = \begin{bmatrix}\sigma^s_0 & \mathcal{H}^s & \mathcal{H}^s_h & \mathcal{H}^s_{tw} & h^s_{\mathsf{L}} & h^s_{\mathsf{T}} & h^s_{\mathsf{LT}} & h^s_{\mathsf{LS}} & h^s_{\mathsf{TS}}\end{bmatrix} \tag{B.2a}$$

$$\mathcal{Y}_h = \begin{bmatrix}\sigma^h_0 & Q^h & b^h & \mathcal{H}^h_s & \mathcal{H}^h_{tw} & h^h_{\mathsf{L}} & h^h_{\mathsf{T}} & h^h_{\mathsf{LT}} & h^h_{\mathsf{LS}} & h^h_{\mathsf{TS}}\end{bmatrix} \tag{B.2b}$$

$$\mathcal{Y}^{\mathrm{hardening}}_{tw} = \begin{bmatrix}\sigma^{tw}_0 & Q^{tw} & b^{tw} & \mathcal{H}^{tw}_s & \mathcal{H}^{tw}_h\end{bmatrix} \tag{B.2c}$$

$$\mathcal{Y}^{\mathrm{yielding}}_{tw} = \begin{bmatrix}C^{tw}_{\mathsf{LT}} & C^{tw}_{\mathsf{LS}} & C^{tw}_{\mathsf{T}} & C^{tw}_{\mathsf{TS}} & C^{tw}_{\mathsf{S}} & C^{tw}_{\mathsf{LT}} & C^{tw}_{\mathsf{LS}} & C^{tw}_{\mathsf{TS}} & k\end{bmatrix} \tag{B.2d}$$

In Eq. (8), we set $a = 4$ (Kondori et al., 2019), and $-1 \le k \le 1$ to satisfy convexity condition for the asymmetric yield function (Cazacu et al., 2006).

The calibration strategy for the parameter set $\mathcal{Y}$ presented above is informed by the CP observations (Indurkar et al., 2020) on the deformation activity of the different modes for each loading scenario. The restriction on the non-dominant mode is realized via

[1] https://1drv.ms/u/s!AkrBMGgaw0Pq7EYdy5Xs0KsK0cbc?e=tLbUEa

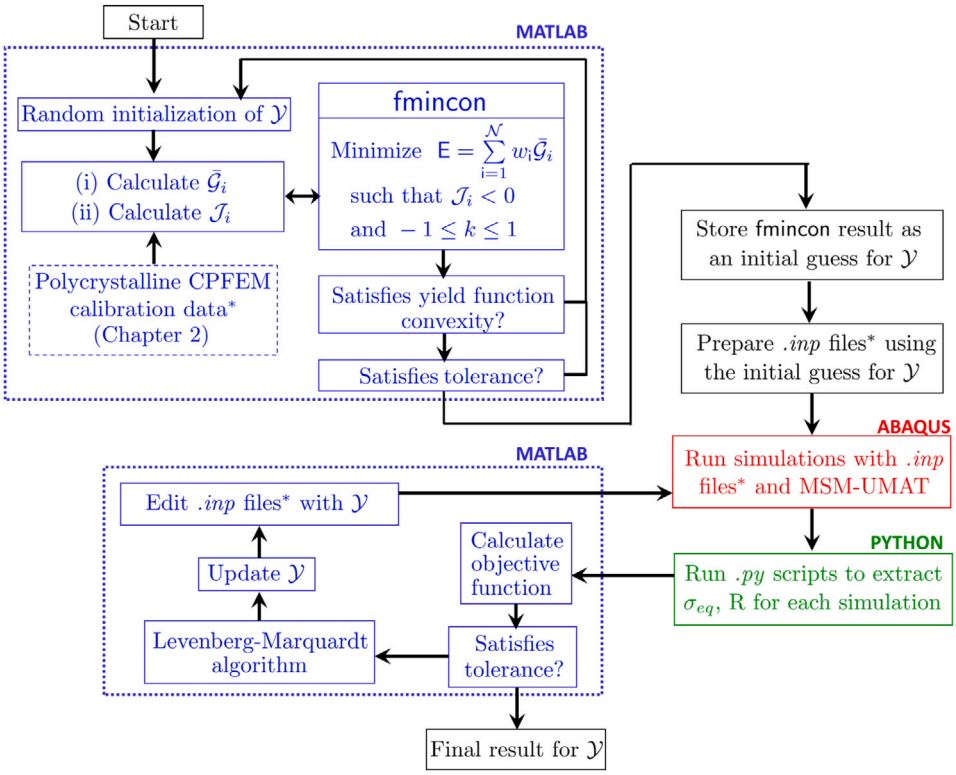

Fig. 15. Two step methodology to calibrate $\mathcal{Y}$ for a given polycrystalline CP simulation dataset. Here * denotes that the data considered includes tension and compression along L, T, S, LT, LS and TS. Chapter 2 refers to the Chapter in Indurkar (2020).

the non-linear conditions ($\mathcal{J}_i$), which in turn ensure the activation of the expected and dominating modes. Thus, the active modes are calibrated to the CP responses.

The parameter set $\mathcal{Y}$ is calibrated to the polycrystal CP simulations corresponding to Texture E in Indurkar et al. (2020). We adopt a two-stage calibration: In stage-I (Fig. 15), Eq. (B.1) is solved using fmincon function from MATLAB optimization toolbox using interior-point algorithm, and results in an *approximately* calibrated MSM. We use a central difference gradient approximation. Moreover, the symmetric positive definiteness for $\mathbb{h}^s$ and $\mathbb{h}^h$ is evaluated using Cholesky Factorization function (chol) in MATLAB.

The values for the set $\mathcal{Y}$ obtained from Stage-I are then used as initial guesses for stage II, which invokes the Levenberg–Marquardt algorithm (MATLAB) together with MSM-UMAT within ABAQUS®, Fig. 15. Note that, unlike Stage-I here no information about the deformation mode activities is used. The objective function vector in this stage is straightforward and is calculated using the relative squared difference between stress and Lankford ratios from the CP simulation, and the corresponding case in the MSM simulation. Using this two-stage calibration protocol, Table 1 consolidates the calibrated parameters for the dataset corresponding to full-field crystal plasticity simulations for texture E (Indurkar et al., 2020).

Appendix C. Supplementary data

Supplementary material related to this article can be found online at https://doi.org/10.1016/j.jmps.2023.105302.

References

Ando, D., Koike, J., Sutou, Y., 2014. The role of deformation twinning in the fracture behavior and mechanism of basal textured magnesium alloys. Mater. Sci. Eng. A 600, 145–152.
Barlat, F., Lege, D.J., Brem, J.C., 1991. A six-component yield function for anisotropic materials. Int. J. Plast. 7, 693–712.
Becker, R., Lloyd, J., 2016. A reduced-order crystal model for HCP metals: application to Mg. Mech. Mater. 98, 98–110.
Benzerga, A.A., Besson, J., 2001. Plastic potentials for anisotropic porous solids. Eur. J. Mech. A Solids 20, 397–434.
Bron, F., Besson, J., 2004. A yield function for anisotropic materials application to aluminium alloys. Int. J. Plast. 20, 937–963.
Cazacu, O., Plunkett, B., Barlat, F., 2006. Orthotropic yield criterion for hexagonal closed packed metals. Int. J. Plast. 22, 1171–1194.
Chandola, N., Lebensohn, R.A., Cazacu, O., Revil-Baudard, B., Mishra, R.K., Barlat, F., 2015. Combined effects of anisotropy and tension–compression asymmetry on the torsional response of AZ31 Mg. Int. J. Solids Struct. 58, 190–200.
Crépin, J., Bretheau, T., Caldemaison, D., 1996. Cavity growth and rupture of β-treated zirconium: A crystallographic model. Acta Mater. 44, 4927–4935.
Hill, R., 1948. A theory of the yielding and plastic flow of anisotropic metals. Proc. R. Soc. Lond. Ser. A Math. Phys. Eng. Sci. 193, 281–297.

Indurkar, P.P., 2020. On the multiscale mechanics of deformation, stability and damage in magnesium. National University of Singapore (Singapore).
Indurkar, P.P., Baweja, S., Perez, R., Joshi, S.P., 2020. Predicting textural variability effects in the anisotropic plasticity and stability of hexagonal metals: Application to magnesium and its alloys. Int. J. Plast. 132, 102762.
Kelley, E.W., Hosford, W.F., 1967. The plastic deformation of magnesium: technical report.
Kim, J.H., Kim, D., Lee, Y.-S., Lee, M.-G., Chung, K., Kim, H.-Y., Wagoner, R.H., 2013. A temperature-dependent elasto-plastic constitutive model for magnesium alloy AZ31 sheets. Int. J. Plast. 50, 66–93.
Koike, J., Ohyama, R., 2005. Geometrical criterion for the activation of prismatic slip in AZ61 Mg alloy sheets deformed at room temperature. Acta Mater. 53, 1963–1972.
Kondori, B., Benzerga, A.A., 2014. Effect of stress triaxiality on the flow and fracture of Mg alloy AZ31. Metall. Mater. Trans. A 45, 3292–3307.
Kondori, B., Madi, Y., Besson, J., Benzerga, A.A., 2019. Evolution of the 3D plastic anisotropy of HCP metals: Experiments and modeling. Int. J. Plast. 117, 71–92.
Koplik, J., Needleman, A., 1988. Void growth and coalescence in porous plastic solids. Int. J. Solids Struct. 24, 835–853.
Lee, J., Kim, S.-J., Lee, Y.-S., Lee, J.-Y., Kim, D., Lee, M.-G., 2017. Distortional hardening concept for modeling anisotropic/asymmetric plastic behavior of AZ31B magnesium alloy sheets. Int. J. Plast. 94, 74–97.
Lee, J.-Y., Steglich, D., Lee, M.-G., 2018. Fracture prediction based on a two-surface plasticity law for the anisotropic magnesium alloys AZ31 and ZE10. Int. J. Plast. 105, 1–23.
Lee, M.-G., Wagoner, R., Lee, J., Chung, K., Kim, H., 2008. Constitutive modeling for anisotropic/asymmetric hardening behavior of magnesium alloy sheets. Int. J. Plast. 24, 545–582.
Li, M., Lou, X., Kim, J., Wagoner, R., 2010. An efficient constitutive model for room-temperature, low-rate plasticity of annealed Mg AZ31B sheet. Int. J. Plast. 26, 820–858.
Muhammad, W., Mohammadi, M., Kang, J., Mishra, R.K., Inal, K., 2015. An elasto-plastic constitutive model for evolving asymmetric/anisotropic hardening behavior of AZ31B and ZEK100 magnesium alloy sheets considering monotonic and reverse loading paths. Int. J. Plast. 70, 30–59.
Nemcko, M.J., Li, J., Wilkinson, D.S., 2016. Effects of void band orientation and crystallographic anisotropy on void growth and coalescence. J. Mech. Phys. Solids 95, 270–283.
Nemcko, M.J., Wilkinson, D.S., 2016. On the damage and fracture of commercially pure magnesium using x-ray microtomography. Mater. Sci. Eng. A 676, 146–155.
Nixon, M.E., Cazacu, O., Lebensohn, R.A., 2010a. Anisotropic response of high-purity α-titanium: Experimental characterization and constitutive modeling. Int. J. Plast. 26, 516–532.
Nixon, M.E., Lebensohn, R.A., Cazacu, O., Liu, C., 2010b. Experimental and finite-element analysis of the anisotropic response of high-purity α-titanium in bending. Acta Mater. 58, 5759–5767.
Peirce, D., Shih, C.F., Needleman, A., 1984. A tangent modulus method for rate dependent solids. Comput. Struct. 18, 875–887.
Plunkett, B., Cazacu, O., Barlat, F., 2008. Orthotropic yield criteria for description of the anisotropy in tension and compression of sheet metals. Int. J. Plast. 24, 847–866.
Plunkett, B., Cazacu, O., Lebensohn, R., Barlat, F., 2007. Elastic-viscoplastic anisotropic modeling of textured metals and validation using the Taylor cylinder impact test. Int. J. Plast. 23, 1001–1021.
Plunkett, B., Lebensohn, R., Cazacu, O., Barlat, F., 2006. Anisotropic yield function of hexagonal materials taking into account texture development and anisotropic hardening. Acta Mater. 54, 4159–4169.
Revil-Baudard, B., Cazacu, O., Flater, P., Kleiser, G., 2015. Plastic deformation of high-purity α-titanium: Model development and validation using the Taylor cylinder impact test. Mech. Mater. 80, 264–275, Materials and Interfaces.
Selvarajou, B., Joshi, S.P., Benzerga, A.A., 2017. Three dimensional simulations of texture and triaxiality effects on the plasticity of magnesium alloys. Acta Mater. 127, 54–72.
Selvarajou, B., Joshi, S.P., Benzerga, A.A., 2019. Void growth and coalescence in hexagonal close packed crystals. J. Mech. Phys. Solids 125, 198–224.
Selvarajou, B., Kondori, B., Benzerga, A.A., Joshi, S.P., 2016. On plastic flow in notched hexagonal close packed single crystals. J. Mech. Phys. Solids 94, 273–297.
Selvarajou, B., Shin, J.-H., Ha, T.K., Choi, I.-s., Joshi, S.P., Han, H.N., 2014. Orientation-dependent indentation response of magnesium single crystals: modeling and experiments. Acta Mater. 81, 358–376.
Shin, J.-H., Kim, S.-H., Ha, T., Oh, K., Choi, I.-S., Han, H., 2013. Nanoindentation study for deformation twinning of magnesium single crystal. Scr. Mater. 68, 483–486.
Simo, J.C., Hughes, T.J., 2006. Computational Inelasticity, vol. 7. Springer Science & Business Media.
Simo, J., Kennedy, J., Govindjee, S., 1988. Non-smooth multisurface plasticity and viscoplasticity. Loading/unloading conditions and numerical algorithms. Internat. J. Numer. Methods Engrg. 26, 2161–2185.
Steglich, D., Tian, X., Besson, J., 2016. Mechanism-based modelling of plastic deformation in magnesium alloys. Eur. J. Mech. A Solids 55, 289–303.
Tari, D.G., Worswick, M., Ali, U., Gharghouri, M., 2014. Mechanical response of AZ31B magnesium alloy: Experimental characterization and material modeling considering proportional loading at room temperature. Int. J. Plast. 55, 247–267.
Yoon, J., Cazacu, O., Mishra, R.K., 2013. Constitutive modeling of AZ31 sheet alloy with application to axial crushing. Mater. Sci. Eng. A 565, 203–212.
Zhang, J., Joshi, S.P., 2012. Phenomenological crystal plasticity modeling and detailed micromechanical investigations of pure magnesium. J. Mech. Phys. Solids 60, 945–972.